

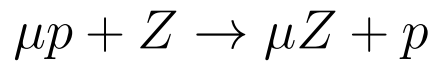


UNIVERSITÀ DEGLI STUDI DI TRIESTE

---

Dipartimento di Fisica  
Corso di Laurea Magistrale in Fisica

# Measurement of the muon transfer rate



with the FAMU experiment

**Laureanda:**  
Elena Furlanetto

**Relatore:**  
Prof. Emiliano Mocchiutti

---

Anno Accademico 2016–2017



## Abstract

La determinazione del raggio del protone è stata una misura importante sin dalla sua scoperta. Le prime misure furono fatte mediante esperimenti di diffusione; in seguito alla scoperta della struttura interna del protone e allo sviluppo della teoria dell'elettrodinamica quantistica sono state formulate due definizioni per il raggio del protone: il raggio di carica e il raggio di Zemach. Queste due grandezze possono essere calcolate con esperimenti di scattering e di spettroscopia, sia con elettroni che con muoni. I muoni sono 200 volte più massivi degli elettroni e quindi il raggio di Bohr per atomi muonici è 200 volte più piccolo. I muoni dunque orbitano più vicino al nucleo atomico rispetto agli elettroni, riuscendo così sondare più da vicino la struttura nucleare. I risultati degli esperimenti di scattering e di spettroscopia, realizzati sia usando muoni che elettroni, sono discordanti fino ad un massimo di  $7\sigma$ . Questa discrepanza ha dato origine al cosiddetto *proton radius puzzle*.

L'obiettivo dell'esperimento FAMU (Fisica Atomi MUonici) è la determinazione del raggio di Zemach del protone mediante la misura dell'energia dello split iperfine dei livelli energetici dello stato fondamentale dell'atomo di idrogeno muonico. L'apparato sperimentale è costituito da un bersaglio di cui si possono regolare la pressione e la temperatura; esso è riempito con una miscela di idrogeno con una contaminazione di un altro elemento ad alto  $Z$ . L'esperimento si trova presso RIKEN-RAL dove viene prodotto un fascio di muoni ad alta intensità. I muoni entrano nel bersaglio dove formano atomi di idrogeno muonico  $\mu p$ ; in seguito alla termalizzazione del sistema viene inviato un impulso laser all'interno del bersaglio in modo da indurre le transizioni singoletto-tripletto del  $\mu p$ . Il  $\mu p$  diseccitandosi emette radiazione ad una energia troppo bassa per essere rivelata direttamente: l'esperimento sfrutta il principio del trasferimento del muone dal  $\mu p$  all'atomo  $Z$  presente nella miscela. Il trasferimento ha una dipendenza dell'energia. In seguito alla diseccitazione del tripletto l'energia cinetica del  $\mu p$  aumenta trasferendo il muone più velocemente all'atomo  $Z$ . L'atomo  $Z$  a questo punto è un atomo mesico in uno stato eccitato che, diseccitandosi, emette radiazione X che può essere rivelata. Quindi, contando il numero di raggi X di diseccitazione dell'atomo  $Z$  in funzione di varie frequenze del laser è possibile ottenere una curva di risonanza centrata al valore di energia dello split iperfine.

L'obiettivo di questo lavoro è lo studio e la determinazione del rate di trasferimento dall'idrogeno muonico ad un atomo ad alto  $Z$  in funzione dell'energia del  $\mu p$  con un rivelatore al germanio. I risultati sono stati confrontati con quelli trovati con l'analisi dei dati raccolti dagli scintillatori al bromuro di lantanio.

**Contributo dell'autore** Nel 2017 sono entrata a far parte della collaborazione dell'esperimento FAMU partecipando all'ultima acquisizione dati presso il Rutherford Appleton Laboratory (UK) e contribuendo alla calibrazione dei rivelatori.

Durante il tirocinio ho studiato e analizzato i dati degli scintillatori al bromuro di lantanio concentrandomi sullo studio della dipendenza della risoluzione in energia dal pile up degli eventi.

L'obiettivo dell'analisi presentata in questa tesi è la determinazione della curva del rate di trasferimento in funzione dell'energia del  $\mu p$ . In particolare ho analizzato per la prima volta i dati raccolti con uno dei quattro rivelatori al germanio. I rivelatori al germanio sono noti per l'ottima risoluzione energetica, essi però sono lenti a causa della formatura del segnale. Per analizzare in modo opportuno i dati è stato necessario introdurre due correzioni, una legata al tempo morto del sistema di acquisizione e una dovuta all'erroneo riconoscimento di eventi in pile up. L'introduzione di una selezione basata sul tempo di salita del segnale ha apportato numerosi vantaggi nella determinazione della curva di correzione.

Dopo aver corretto i dati ho selezionato tre intervalli temporali e per ognuno di essi ho considerato lo spettro energetico dopo avere sottratto il fondo. Per ogni spettro energetico ho calcolato l'integrale in una regione energetica ben determinata e ho realizzato un fit dei valori dell'integrale in funzione del tempo. Il valore del parametro della funzione di fit è il rate di trasferimento. Ripetendo questa procedura per tutte le temperature ho ottenuto la curva del rate di trasferimento in funzione della temperatura.

Il risultato che ho ottenuto è in accordo con i risultati trovati in modo indipendente con gli scintillatori; l'analisi degli errori sistematici evidenzia che il contributo più grande all'errore è dovuto all'incertezza nella sottrazione del fondo.

**Contenuti della tesi** Questa tesi è organizzata in cinque capitoli. Nel primo capitolo è riassunta la storia della scoperta del protone; sono spiegati inoltre i concetti di raggio di carica e raggio di Zemach; per ognuna delle due definizioni sono riportati i risultati sperimentali che hanno contribuito a originare il *proton radius puzzle*. Nel secondo capitolo viene presentato il metodo sperimentale dell'esperimento FAMU, descrivendo più approfonditamente la procedura per la determinazione della curva del rate di trasferimento. Il capitolo tre è dedicato alla descrizione dell'apparato sperimentale: il fascio di muoni, il bersaglio, i rivelatori e il sistema di acquisizione; nello stesso capitolo viene descritta anche la procedura di calibrazione. Il quarto capitolo è dedicato alla spiegazione dell'analisi dati e alla discussione dei risultati ottenuti. L'ultimo capitolo contiene le conclusioni della tesi.

## Abstract

The determination of the proton radius is a challenge since the proton discovery. The first measurements were performed with electron scattering experiments. After the discovery of the proton internal structure and the development of the Quantum Electro-Dynamics (QED) two definitions of the proton radius were formulated: the charge radius and the Zemach one. These quantities can be calculated by means of atomic spectroscopy measurements or scattering experiments. Both these techniques can be applied also with muons: they are 200 times massive than electrons and so the Bohr radius of muonic atoms is 200 smaller; since they orbit closer to proton than electrons, they are more sensitive to the nuclear structure. The present results, both with scattering or spectroscopic measurements, obtained with electrons or muons share a discrepancy up to  $7 \sigma$ . This discrepancy generated the so-called *proton radius puzzle*.

The goal of the FAMU (Fisica Atomi MUonici) experiment is the determination of the proton Zemach radius with the measurement of the hyperfine splitting of the muonic hydrogen ground state. To reach the purpose, the experimental apparatus is made up of a cryogenic and pressurised gas target, filled with a gas mixture of  $H_2$  and another high  $Z$  gas in a small concentration. The experiment is placed at the RIKEN-RAL muon facility where a high intensity muon beam is produced. After the formation and thermalisation of the  $\mu p$ , a laser set on the hyperfine energy is sent to the target inducing a  $\mu p$  singlet to triplet transition. The  $\mu p$  de-excitation X-rays can not be detected directly so the FAMU experiment exploits the energy dependence of the muon transfer rate to high  $Z$  gases. When the  $\mu p$  de-excites from the triplet configuration gains kinetic energy; these energetic  $\mu p$  have a higher probability to transfer their muon to the  $Z$  atom respect to those thermalised. Counting the number of the X-rays emitted by the de-excitation of the  $Z$  atom as function of various laser energies it is possible to obtain a resonance plot peaked at the hyperfine energy value.

The aim of this work is the study and the determination of the transfer rate from muonic hydrogen  $\mu p$  to higher  $Z$  atom as function of the  $\mu p$  energy with HPGe detectors. The obtained results are compared to those found with an independent analysis performed with LaBr3(Ce) scintillators.

**The author's contribution** I joined the FAMU collaboration in 2017; at the beginning of the same year, I participated to the acquisition run at Rutherford Appleton Laboratory (UK). During the campaign I contributed to the detectors calibration.

During the stage activity I calibrated the LaBr3(Ce) scintillators and I studied their behaviour as function of energy; in particular I analysed the pile up events reconstruction.

The aim of this analysis is the determination of the transfer rate curve as function of  $\mu p$  energy. In particular I analysed for the first time the data acquired with the fast shaped output of a HPGe. The HPGes have optimal energy resolution however they are slow for high rate counting experiments, so the data analysis required two important corrections: one due to the saturation of the acquisition system and the other due to the pile up events. Both these aspects cause the loss of good events, so the corrections are necessary. The introduction of a rise time selection to determine the pile up events makes easier the construction of the pile up rejection curve.

After the data correction I selected three time intervals and for each of them I subtracted the background and then I counted the number of detected X-rays. The dependence of the integral as function of time is fitted with a proper function; the fit parameter determines the transfer rate.

I repeated this procedure for all the temperatures and I obtained the transfer rate curve. The result is in agreement with the one obtained with the LaBr3(Ce) scintillators at the same experimental conditions. The analysis of the systematic errors outlines the necessity of a better background estimation, since the largest systematic error component is due to the background subtraction.

**Outline of this thesis** This thesis is organised in five chapters; in the first chapter I make a general description of the proton history. I explain the concepts of charge and Zemach radius with the relevant theoretical calculations; for each definition I also present some experimental results that gave origin to the *proton radius puzzle*. In the second chapter, I describe the FAMU experimental method giving large space to the transfer rate curve determination. The third chapter is dedicated to the description of the FAMU experimental apparatus: the muon beam, the gas target, the detectors and the acquisition system. The calibration procedure is also described. The fourth chapter is devoted to the explanation of the data analysis and to the discussion of the measurement results. In the last chapter, the conclusions of this work are summarised.

# Contents

<b>1</b>	<b>Proton structure: theory and measurements</b>	<b>3</b>
1.1	Introduction . . . . .	3
1.2	Charge radius . . . . .	5
1.2.1	Charge radius determination via scattering experiments . .	5
1.2.2	Results from scattering experiments . . . . .	8
1.2.3	Charge radius via atomic spectroscopy . . . . .	9
1.2.4	Results from hydrogen atom spectroscopy . . . . .	12
1.3	Zemach radius . . . . .	13
1.3.1	Hyperfine splitting and Zemach radius theory . . . . .	13
1.3.2	Zemach radius results . . . . .	16
1.3.3	Future perspectives: the FAMU experiment . . . . .	17
<b>2</b>	<b>FAMU experimental method</b>	<b>19</b>
2.1	The FAMU concept . . . . .	19
2.2	Prompt phase: muonic atom formation and thermalisation . . . .	21
2.3	Delayed phase: laser excitation and hyperfine splitting measurement	23
2.4	Transfer rate measurement . . . . .	24
<b>3</b>	<b>Experimental apparatus</b>	<b>29</b>
3.1	Muon beam . . . . .	29
3.2	Gas target . . . . .	30
3.3	Detectors . . . . .	32
3.3.1	Lanthanum Bromide Scintillators . . . . .	32
3.3.2	High Purity Germanium detectors . . . . .	34
3.3.3	Hodoscope . . . . .	38
3.4	Data acquisition and control . . . . .	41
3.5	HPGe wave form analysis . . . . .	41
3.6	Temperature control . . . . .	42
<b>4</b>	<b>Data analysis</b>	<b>45</b>
4.1	Dead time correction . . . . .	46
4.2	Pile up rejection selection . . . . .	48
4.2.1	Rise time of calibration data . . . . .	48
4.2.2	Rise time of beam data . . . . .	51
4.3	Pile up rejection cut efficiency . . . . .	56

4.4	Transfer rate measurement . . . . .	59
4.4.1	Background subtraction . . . . .	59
4.4.2	Peak identification . . . . .	61
4.5	Fit function . . . . .	62
4.5.1	Parameters determination . . . . .	64
4.5.2	Fit of the data . . . . .	65
4.6	Systematic errors estimation . . . . .	66
4.6.1	Background subtraction . . . . .	66
4.6.2	Efficiency correction . . . . .	67
4.6.3	Concentration of gas mixture . . . . .	67
4.6.4	Temperature . . . . .	67
4.6.5	$t_{th}$ uncertainty . . . . .	67
4.6.6	Other systematics . . . . .	67
4.7	Results discussion . . . . .	68
<b>5</b>	<b>Conclusions</b>	<b>69</b>

# Chapter 1

## Proton structure: theory and measurements

### 1.1 Introduction

The proton is one of the building blocks of ordinary matter. At the beginning of the XX century the structure of atoms was not known in details. In 1909 H. Geiger and E. Marsden [1], with the collaboration of Lord Rutherford, performed an experiment by colliding  $\alpha$  particles on a thin gold absorber to test the validity of the plum-pudding model proposed by Thomson [2].

The plum-pudding model describes the atom as a neutral spherical volume, in which there is the same number of positive and negative charges; the positive charge is represented by the plum. If the volume is completely full, the incoming radiation should be scattered back.

Geiger and Marsden observed that  $\alpha$  particles, that are helium nuclei, were scattered back with a large deflection angle or they passed through the absorber maintaining the initial trajectory.

The explanation they gave is that the atom is formed by a charged nucleus that is confined in a small region; the negative charges are orbiting around the nucleus maintaining the neutrality of the atom. Only if the  $\alpha$  particle interacts with the nucleus it is scattered back, otherwise it continues on its path.

Some years later, in 1919, Lord Rutherford discovered the proton as the product of the  $^{14}\text{N} + \alpha \rightarrow ^{17}\text{O} + \text{p}$  reaction. He deduced that protons are the fundamental positive charges present in the atomic nucleus [3].

After the development of the Quantum Chromo Dynamics (QCD) and the discovery of the quarks, it was found that also the proton has a composite structure composed of three quarks, two up and one down, called valence quarks, and of many others quarks, called *sea quarks*.

Since the proton has not a well defined physical structure it is not possible to define an unique physical quantity for its size. Up to now there are two definitions: the charge radius, that takes into account the proton charge distribution, and the Zemach radius that considers both the charge and magnetic distributions. Proton

structure can be studied by looking at its interactions with  $e^-$  and  $\mu^-$ . Electrons are fundamental particles, with 0.511 MeV mass and spin 1/2; electrons are point-like and they interact only electromagnetically, they are suitable to probe the nuclear structure.

Muons belong to the leptons family; they have a mass equal to 105.65 MeV, about 200 times greater than the electron one. Muons are unstable particles, they can decay in electrons and neutrinos with a life time of about 2.2  $\mu$ s in vacuum or can undergo nuclear capture (details are reported in chapter 3). A muon has the same properties of electron in terms of electric charge (-1 in elementary charge unit) and spin (1/2).

An atom in which one of the electrons is replaced by a muon is called muonic atom. In particular, if we consider the hydrogen atom, that has the simplest atomic structure because it is composed of one electron and one proton, the mean radius of each orbit is given by

$$\langle r \rangle = \frac{a_B}{2}(3n^2 - l(l - 1)), \quad (1.1)$$

where  $n = 1, 2, \dots, \infty$  is the principal quantum number,  $l = 0, \dots, n - 1$  is the orbital angular momentum and  $a_B$  is the Bohr radius divided by the system reduced mass  $\mu$  to take into account the nucleus finite dimension.  $a_B$  depends on the electron mass and it is given by

$$a_B = \frac{\hbar^2(m_e + M)}{m_e M e^2}, \quad (1.2)$$

from which it can be seen the inverse proportionality of the orbit radius with respect to the electron mass  $m_e$ .

If instead of the electron there is a muon in orbit around the nucleus, since the muon mass is 200 times greater than the electron mass, the orbit radius will be shorter and the bounding energy will be greater ( $E_B \propto 1/\langle r \rangle$ ). Exploiting these properties, muons can be used to probe the atom nucleus structure and, in case of hydrogen, the proton.

Studying the proton structure is one of the possible ways to test the validity of the Quantum Electro-Dynamics (QED). The QED describes the processes that involve the electromagnetic force between particles. It is one of the most complete and well known theories: it predicts the muon anomalous magnetic moment and the Lamb shift.

In 2010 in an article published by Nature, Pohl and collaborators [4] pointed out a discrepancy between the values of the proton charge radius found with scattering experiments and their result, obtained measuring the Lamb shift of muonic hydrogen. Their result is  $\langle r_p \rangle = 0.84184 \pm 0.00067$  fm whereas the one reported by CODATA (Committee on Data for Science and Technology) [5], after combining the results obtained from different experiments, is  $\langle r_p \rangle = 0.8768 \pm 0.0069$  fm.

This discrepancy, called *proton radius puzzle*, combined with the interest of a deep understanding of the QED gave the boost for a improvement of the research in the nuclear field.

Since the proton has a composite structure made up of three valence quarks interacting by gluons exchange, it is not possible to define a unique radius. The proton radius, both the charge and the Zemach one, can be obtained in two ways: by a direct measurement of the electric and magnetic form factors with lepton - proton scattering, or indirectly, by means of spectroscopic measurements of hydrogen atom.

## 1.2 Charge radius

The proton charge radius is calculated considering only the proton charge distribution.

### 1.2.1 Charge radius determination via scattering experiments

H. Geiger and E. Marsden used, in their experiment,  $\alpha$  particles to test the nuclear structure [1]. However, a better way to probe the nuclear structure is to use elementary particles, as electrons or muons, because they are point-like and they interact only electromagnetically ( $\alpha$  particles have a composite structure and interact also with the strong force).

The starting point for a theoretical treatment of the scattering experiments is the Rutherford scattering formula:

$$\frac{d\sigma}{d\Omega_R} = \left(\frac{Z\alpha}{2E}\right)^2 \frac{1}{\sin^4(\theta/2)}, \quad (1.3)$$

in which  $Z$  is the nucleus atomic number,  $\alpha = 1/137$  is the fine structure constant,  $E$  is the electron energy and  $\theta$  is the electron deflection angle respect to the incoming direction.

This formula is valid under some hypotheses:

- electrons and protons are spinless and point-like particles;
- the proton has infinite mass;
- the scattering interaction is elastic, non relativistic and the only acting force is the Coulomb one;
- the validity of the Born approximation:  $Z_1 Z_2 \alpha \ll 1$ , in which  $Z_1$  and  $Z_2$  are the charge of the incoming charge particle and of the nucleus respectively.

To study the dimension of the proton order of fm, the electron must have an energy of about 200 MeV in order to respect the interaction scale that is given by the Compton wavelength  $\lambda = \hbar c \approx 200 \text{ MeV} \cdot \text{fm}$ . At such energy the electron is relativistic.

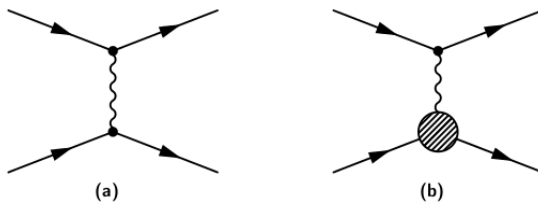


Figure 1.1: Feynman diagrams representing the interaction of an electron with a massive point-like particle (a) and the electron proton interaction (b) [7].

To take into account the relativistic correction to the cross section, we consider the electron spin and the nucleus recoil. The result is the Mott cross section [6]:

$$\frac{d\sigma}{d\Omega_M} = \left(\frac{d\sigma}{d\Omega}\right)_R (1 - \beta^2 \sin^2 \theta / 2), \quad (1.4)$$

where  $\beta = v/c$  is the electron velocity in units of speed of light. If  $\theta = 2\pi$  the Mott cross section is zero; this is a consequence of the helicity conservation in electromagnetic interactions. The helicity is the projection of the spin vector  $\sigma$  on the particle momentum; for the electron it could be  $\pm 1$ . However, helicity is conserved in electromagnetic interactions so the electron has to maintain its initial helicity value. If the electron is scattered at  $\theta = 2\pi$  its helicity changes violating the selection rule.

The description given by the Mott cross section can be improved introducing the proton spin; therefore the electron will interact both with the proton charge and magnetic moment. The calculations were done by Rosenbluth that introduced two form factors, one for the charge distribution and one for the magnetic moment. The Rosenbluth cross section is:

$$\left(\frac{d\sigma}{d\Omega}\right)_{Rosen} = \left(\frac{d\sigma}{d\Omega}\right)_{Mott} \left[ A(q^2) + B(q^2) \cdot \tan^2 \left(\frac{\theta}{2}\right) \right]. \quad (1.5)$$

However, in this interpretation, the proton is still point-like. To obtain a relation between scattering parameters and proton radius it is necessary to introduce some QED concepts.

In QED the particle interaction can be described using the Feynman diagrams. The interaction of an electron with a massive point-like particle is represented in figure 1.1(a); the electron proton interaction, in terms of Feynman diagram is represented in figure 1.1(b). The two particles interact via photon exchange and the composite structure of the proton implies the presence of a different proton-photon interaction vertex respect to the electron-photon one.

The matrix element of the interaction is:

$$M_{fi} = J_{\mu}^{elec} \frac{1}{q^2} J_{prot}^{\mu}, \quad (1.6)$$

where

$$J_\mu^{elec} = -e \cdot \bar{u}(k') \gamma_\mu \cdot u(k) \quad (1.7)$$

is the electron current and

$$J_{prot}^\mu = e \cdot \bar{u}(p') \Gamma^\mu \cdot u(p) \quad (1.8)$$

is the proton current;  $(k, k')$  and  $(p, p')$  are the initial and final four-momentum of the electron and proton,  $u(k)$  and  $u(p)$  are the spinors associated to electron and proton respectively. The exchange four momentum is  $q = k - k'$ .

$J_{prot}^\mu$  must be a Lorentz four-vector. Using the Gordon decomposition the most general form for  $\Gamma^\mu$  is:

$$\Gamma^\mu = \left[ F_1(q^2) \gamma^\mu + \frac{\kappa}{2m_p} F_2(q^2) i \sigma^{\mu\nu} q_\nu \right], \quad (1.9)$$

with  $\sigma^{\mu\nu} = \frac{i}{2} [\gamma^\mu \gamma^\nu]$ . The first term is the result of the electric interaction whereas the second is the result of the magnetic one;  $m_p$  is the proton mass. The cross section is obtained by calculating the modulus squared of the matrix element and by summing over the final spins and averaging on the initial ones. The final result for the Rosenbluth cross section is:

$$\left( \frac{d\sigma}{d\Omega} \right)_{Rosen} = \left( \frac{d\sigma}{d\Omega} \right)_{Mott} \left\{ \left[ F_1(q^2) - \frac{\kappa^2 q^2}{4m_p^2} F_2(q^2) \right] - \frac{q^2}{2m_p} \left[ F_1(q^2) - \kappa F_2(q^2) \right] \tan^2 \left( \theta/2 \right) \right\}, \quad (1.10)$$

where  $F_1(q^2)$  and  $F_2(q^2)$  are the two form factors and  $\kappa$  is the proton magnetic moment.

This formula can be rewritten introducing the proton electric and magnetic form factors  $G_E$  and  $G_M$ :

$$G_E = F_1 + \frac{\kappa q^2}{4m_p^2} \cdot F_2, \quad (1.11)$$

$$G_M = F_1 + \kappa \cdot F_2. \quad (1.12)$$

The Rosenbluth cross section becomes:

$$\left( \frac{d\sigma}{d\Omega} \right)_{Rosen} = \left( \frac{d\sigma}{d\Omega} \right)_{Mott} \left\{ \frac{G_E^2(Q^2) + \tau G_M^2(Q^2)}{1 + \tau} + 2\tau G_M^2(Q^2) \tan^2 \theta/2 \right\}, \quad (1.13)$$

in which  $Q^2 = -q^2$  and  $\tau = Q^2/(4m_p^2)$ . The electric form factor  $G_E$  describes the proton electric charge distribution whereas the magnetic form  $G_M$  describes its magnetic dipole moment distribution.

The behaviour of  $G_E$  and of  $G_M$  as function of  $Q^2$  can be described with a dipole function:

$$G_E(q^2) = \left( \frac{1}{1 + (q^2/0.71)} \right)^2, \quad (1.14)$$

where  $q^2$  is expressed in  $(\text{GeV}/c)^2$ .

The Fourier transform of the proton charge density  $\rho(\mathbf{r})$  is directly connected to the form factor:

$$G_E(q^2) = \int \rho(\mathbf{r}) \cdot e^{i\mathbf{q}\cdot\mathbf{r}} d\mathbf{r}. \quad (1.15)$$

Expanding this equation for  $q^2 \rightarrow 0$  you get:

$$G_E^p(q^2) \approx \int [1 + i\mathbf{q} \cdot \mathbf{r} - \frac{1}{2}(\mathbf{q} \cdot \mathbf{r})^2 + \dots] \rho(\mathbf{r}) \quad (1.16)$$

$$= Q(0) - \frac{1}{6} Q^2 \int r^2 \rho(\mathbf{r}) d\mathbf{r} + \dots \quad (1.17)$$

$$= Q(0) - \frac{1}{6} Q^2 \langle r^2 \rangle + \dots, \quad (1.18)$$

where  $Q(0) = 1$  is the proton charge. From the last relation, it is possible extract the mean squared value of the proton charge radius:

$$\langle r_E^2 \rangle = - \frac{6}{G_E(0)} \left. \frac{dG_E(Q^2)}{dQ^2} \right|_{Q^2=0}. \quad (1.19)$$

A similar procedure can be followed to obtain the relation between the magnetic form factor and the mean squared magnetic radius:

$$\langle r_M^2 \rangle = - \frac{6}{G_M(0)} \left. \frac{dG_M(Q^2)}{dQ^2} \right|_{Q^2=0}. \quad (1.20)$$

The electric and magnetic form factors can be determined via scattering experiments exploiting the relation reported in equation 1.5. At fixed  $q^2$  value, the differential cross section as function of the deflection angle  $\theta$  is studied. In figure 1.2 is shown a typical plot of the differential cross section versus the scattering angle. Comparing the experimental curve with the equation 1.5, it can be noticed that the slope represents the  $B(Q^2)$  value whereas the y-intercept the  $A(Q^2)$  one. The theoretical expression for  $A(Q^2)$  and  $B(Q^2)$  can be inferred by analogy from equation 1.13; finally, from  $A(Q^2)$  and  $B(Q^2)$  it is possible calculate the two form factors and then the mean charge radius.

## 1.2.2 Results from scattering experiments

One of the most recent experiment devoted to the proton charge radius measurement with e-p scattering was performed at MAMI (MAInz MIcrotron) in 2010 [9]: the A1 collaboration exploited three high resolution spectrometers with a large acceptance (28 msr) and angular resolution (3 mrad). The aim of the experiment was to infer the form factors at  $Q^2 = 0.6$  (GeV/c)<sup>2</sup>. The proton charge radius they measured is:

$$\langle r_E^2 \rangle^{1/2} = 0.879 \pm 0.005_{stat} \pm 0.004_{syst} \pm 0.002_{model} \pm 0.004_{group} \text{ fm}. \quad (1.21)$$

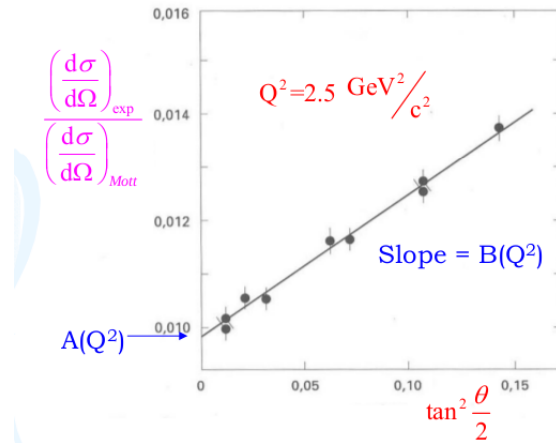


Figure 1.2: On y-axis: the values of the cross section ratio between the experimental values and the theoretical ones. On x-axis: a function of the deflection angle. The linear relation between these two quantities permits to extrapolate the value of the charge radius [8].

Another e-p scattering experiment was proposed in 2011 at Jefferson Laboratory [10]. Actually the proton radius they found is:  $\langle r_E^2 \rangle^{1/2} = 0.875 \pm 0.009$  fm.

To verify the theory and the experimental results found with e-p scattering, new test can be done studying the  $\mu$ -p scattering. In the past (around '70 and '80) some test were performed but they extracted the proton radius with an insufficient precision. In current years a new experiment is proposed: the MUon Scattering Experiment (MUSE) at the Paul Scherrer Institute (PSI) [11]. The collaboration aims to evaluate the proton radius using both positive and negative muons in a  $Q^2$  range of about 0.002 - 0.07  $\text{GeV}^2$ . In figure 1.3, the values of the root mean square of the proton charge radius found in different experiments are shown: on the left the predicted values for the  $\mu$ -p scattering, on the right the values obtained from experiments. The black point represents the CODATA value. There is a discrepancy up two  $7 \sigma$  between the  $\mu$ -p and e-p results.

### 1.2.3 Charge radius via atomic spectroscopy

The proton charge radius can also be extracted from hydrogen atom spectroscopy.

The hydrogen atom is one of the most studied atomic systems because of its structure: it is an electron-proton bound state and it can be described very accurately.

The first description of hydrogen atom considered the proton mass infinitely large ( $m_e/m_p = 1/2000$ ) and assumed a central Coulomb potential generated by the nucleus. With these assumptions, the energy levels, resulting from the Schrödinger equation, depend only on the principal quantum number  $n$  and they are degenerate on  $l$ :

$$E_n = -m_e c^2 \frac{(Z\alpha)^2}{2n^2}. \quad (1.22)$$

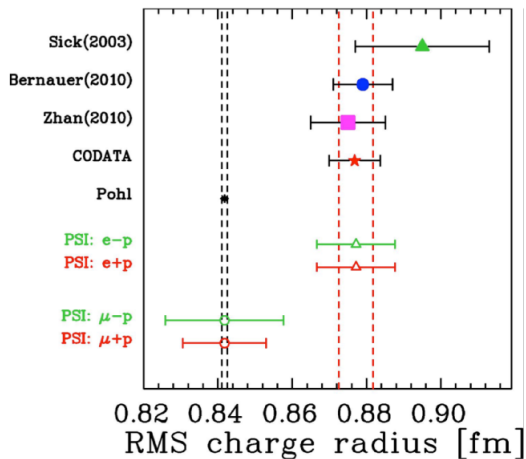


Figure 1.3: Graphic representation of the experimental results for charge radius from [12]: results expected from PSI for  $\mu$ -p and e-p scattering with other experimental results.

In order to consider the mass  $M$  of the nucleus in equation 1.22 the mass  $m_e$  has to be substituted with the reduced mass  $\mu$ .

The Rydberg constant, that is one of the fundamental values in atomic and molecular physics, is defined as:

$$R_\infty = \alpha^2 \frac{m_e c^2}{2\hbar c}. \quad (1.23)$$

The Rydberg constant is the inverse of a length and represents the minimum wave number of a photon that can be emitted from the hydrogen atom ground state leaving it ionised. The differences in the proton charge radius results could be due to an imprecise evaluation of the Rydberg constant.

In order to consider the electron spin ( $1/2$ ) and its energy dependence on the momentum a relativistic approach is necessary. This was done by Dirac which found that states with the same  $n$  but different total angular momentum  $j$  are splitted into  $n$  components. In the Dirac formula for the energy level several corrections are taken into account considering also the correction due to finite mass  $M$  of the nucleus.

In 1947, Lamb and Retherford measured for the first time the  $2S_{1/2} - 2P_{1/2}$  energy splitting that is called *Lamb shift* [13]. The *Lamb shift* correction to the energy levels includes corrections that are not considered in Dirac equation solutions. The Lamb shift can be described by means of a quantum field treatment using the Feynman diagrams. The four main contributions to the Lamb shift are [14]:

- radiative: this contribution is due to QED effects as self-energy and vacuum polarization for an electron in a Coulomb potential of an infinity heavy and point like nucleus; it depends on  $\alpha$  and  $Z\alpha$ ;

- recoil: it depends on  $Z\alpha$  and on  $m_e/M$  and it arises from the exchange of two or more photons between electron and proton;
- radiative-recoil: it is a mixture of both the two previous;
- finite nuclear size: it derives from considering the nucleus as an extended object with a structure. Another contribute is due to the nucleus polarization.

The radiative corrections are the largest one and the correction relevant for the proton radius determination is the finite nuclear size correction.

The atom energy levels shift is due to the finite size of the proton which electric field can not be described with a Coulomb potential but with a potential that depends on the charge distribution inside the nucleus.

If one describes the nucleus potential as a Coulomb potential with a perturbation term, as [14]:

$$\delta V(\mathbf{r}) = V(\mathbf{r}) - \left( -\frac{Z\alpha}{r} \right), \quad (1.24)$$

and remembering that the charge form factor is the Fourier transform of the nucleus ground state charge density (see equation 1.15), after some calculations, the correction to the nucleus potential can be written as:

$$\delta V(r) = \frac{2\pi(Z\alpha)}{3} r_p^2 \delta(r) - \frac{Q\alpha}{2r^3} \frac{3(\mathbf{S} \cdot \hat{\mathbf{r}})^2 - \mathbf{S}^2}{S(2S-1)} + \dots, \quad (1.25)$$

where  $Z$  is the atomic number,  $r_p^2$  is the proton squared mean radius,  $Q$  is the nuclear quadrupole moment. If we consider the hydrogen atom in which  $Z = 1$ , the proton spin is  $1/2$  that implies  $Q = 0$ , the second term of the perturbation expansion vanishes and the relevant contribution to the energy shift is given by the first term.

Using the non-relativistic Schrödinger wave function  $\Psi(r)$  and the perturbation theory, the hydrogen level energy correction is  $\Delta E = \langle \bar{\Psi}(r) | \delta V | \Psi(r) \rangle$ :

$$\Delta E = \frac{2\pi(Z\alpha)}{3} r_p^2 |\Psi_n(0)|^2 = \frac{2(Z\alpha)^4}{3n^3} \mu^3 r_p^2 \delta_{l0} \simeq 1162(51) \frac{\delta_{l0}}{n^3} \text{ kHz}. \quad (1.26)$$

Since the energy shift depends on  $\delta_{l0}$ , it is different from zero only for S states. The equation 1.26 is not the final expression because others contributions coming from Feynman diagrams are to be added; however they are of the  $(Z\alpha)^6$  order, so they are negligible (about 0.7 kHz for the 1S state in hydrogen). For further calculation details see reference [14].

The experimental method to measure the Lamb shift consists in measuring the energy difference between two defined energy levels of hydrogen; by means of theoretical calculations the proton charge radius is obtained.

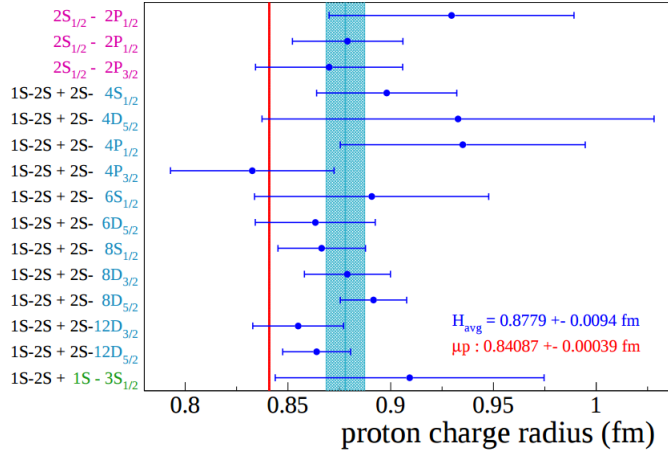


Figure 1.4: Summary of electronic hydrogen spectroscopic measurements of charge radius [15]. The blue shadow represents the uncertainty limit given by CODATA. The red line indicates the value of charge radius extract from muonic hydrogen Lamb shift by CREMA collaboration.

## 1.2.4 Results from hydrogen atom spectroscopy

An overview of the proton charge radius calculated by means of hydrogen atom spectroscopy is presented in figure 1.4. The red line represents the result obtained by measuring the Lamb shift in muonic hydrogen.

The charge radius obtained as the mean value of various experimental results is  $\langle r_E^2 \rangle_{avg}^{1/2} = 0.8779 \pm 0.0094$  fm; the value obtained by CREMA collaboration using muonic hydrogen is  $\langle r_E^2 \rangle_{avg}^{1/2} = 0.84087 \pm 0.00039$  fm. These two values differ of about  $6\sigma$ .

CREMA collaboration measured also the three transitions of the muonic deuterium, that is formed by a deuteron with an orbiting negative muon [16]: the result is  $\langle r_d^2 \rangle^{1/2} = 2.12562 \pm 0.00078$  fm whereas the CODATA result for this transition is  $\langle r_d^2 \rangle^{1/2} = 2.1424 \pm 0.0021$  fm: in this case the two radii differ of  $7.5\sigma$ . The result found by CREMA collaboration is  $3.5\sigma$  smaller than the radius obtained with electronic deuterium. The same collaboration performed also measurements of the muonic helium Lamb shift: the very preliminary results do not share such discrepancy from the theoretical predictions and from the regular helium values [17].

In figure 1.5, a summary of some measurements for the charge radius is presented, considering scattering and spectroscopy results obtained with electrons or muons. The values obtained using muons is about  $6\sigma$  from those obtained using electrons. This can be due to a systematic introduced in the charge radius evaluation when calculated using muons or to the presence of a new physics process currently unknown.

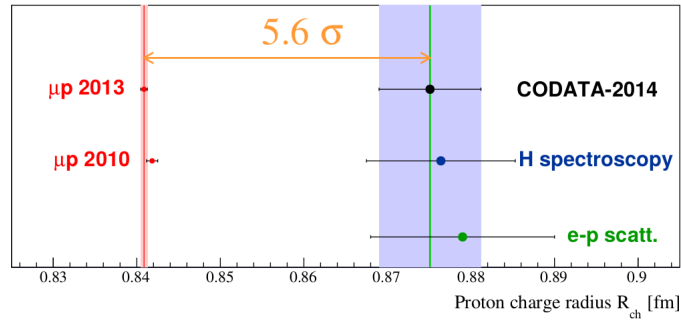


Figure 1.5: Summary of some measurement results of charge radius [15]. The red point are those measured with  $\mu$ -p scattering experiment. The black point is the CODATA result with its uncertainty indicated by the grey shadow, the blue point is an average of hydrogen spectroscopy results and the green point an average on e-p scattering results.

## 1.3 Zemach radius

The Zemach radius is defined as the first moment of the convolution of the electric and the magnetic distributions [18]. It can be obtained by measuring the hydrogen hyperfine energy splitting.

### 1.3.1 Hyperfine splitting and Zemach radius theory

The hyperfine splitting is a consequence of the interaction between the total angular momentum of the nucleus  $\mathbf{I} = \mathbf{L}' + \mathbf{S}'$  and the total angular momentum of the electrons  $\mathbf{J} = \mathbf{L} + \mathbf{S}$  where  $\mathbf{L}, \mathbf{L}'$  are the total orbital momenta and  $\mathbf{S}, \mathbf{S}'$  are the total spin momenta for the electrons and nucleus respectively. The atom energy levels depend on  $\mathbf{F} = \mathbf{I} + \mathbf{J}$ ; this splitting is small, of the order of  $\mu\text{eV}$ , and it is due to the finite size of the nucleus [19].

In particular, the hydrogen atom is made up of one proton ( $\mathbf{S}' = 1/2$ , with eigenvalues  $s' = \pm 1/2$ ,  $l' = 0$ ) and one electron ( $\mathbf{S} = 1/2$ , with eigenvalues  $s = \pm 1/2$ , the value of  $L$  depends on the orbital where the electrons are. If we consider  $n = 2$  and  $l = l' = 0$ , the possible values of  $F$  are  $F = 0, 1$ , so the  $2S$  splits in two energy levels, one for each value of  $F$ . Considering, instead,  $n = 2$ ,  $l = 1$ ,  $l' = 0$ ,  $s' = +1/2$ ,  $s = +1/2$ :

$$|l - s| < j < l + s \rightarrow j = 1/2, 3/2,$$

and if  $i = \pm 1/2$  then

$$\left. \begin{array}{l} j = 1/2 \\ i = \pm 1/2 \end{array} \right\} \rightarrow F = 0, 1$$

$$\left. \begin{array}{l} j = 3/2 \\ i = \pm 1/2 \end{array} \right\} \rightarrow F = 1, 2.$$

Each of the P levels, which depends on the the value of  $j$ , is then separated in other two levels depending on  $F$ .

The same explanation holds if the muon is considered instead of the electron. Infact the muon has the same properties of electron in terms of electromagnetic interactions. The main difference stands in the amplitude of the splitting. In figure 1.6 the comparison between energy levels of the regular hydrogen atom and of the muonic atom is shown. The energy levels split is the same for electrons and muons, the differences are the amplitude of the split and the levels organisation. In regular hydrogen, the Lamb shift between  $2S_{1/2}$  and  $2P_{1/2}$  is three order of magnitude smaller than in muonic hydrogen: this is due to the different contribution of the Feynman diagrams in the calculation of the energy corrections.

The theoretical description of the hyperfine splitting is based on QED; even if it is one of the most accurate theories, the limited precision of the Rydberg and the hyperfine structure constants combined to the unknown contributions coming from higher order perturbations terms and the insufficient knowledge of the proton structure, make the theoretical prevision of the hyperfine energy splitting less precise respect to the experimental value.

The value of the hyperfine energy splitting ( $\Delta E^{hfs}$ ) can be written in an explicit form in which all the contributions appear separately [20]:

$$\Delta E_{th}^{hfs} = E^F (1 + \delta^{QED} + \delta^{struc}) \quad (1.27)$$

$$= E^F (1 + \delta^{QED} + \delta^{Zemach} + \delta^{recoil} + \delta^{pol} + \delta^{hvp}), \quad (1.28)$$

where

$$E^F = \frac{8}{3} \alpha^4 c^3 \frac{m_e^2 m_p^2}{(m_e + m_p)^3} \mu_p \quad (1.29)$$

is the Fermi energy splitting in terms of the electron and proton masses and of the proton magnetic moment  $\mu_p$ ;  $\delta^{QED}$  is due to QED higher order corrections and the remaining terms are related to the proton electromagnetic structure and to its interactions. If the proton is considered point-like  $\delta^{struc}$  would vanish.

$\delta^{QED}$  includes both radiative and relativistic effects and, up to terms of  $\alpha^3$ , it can be expressed as:

$$\delta^{QED} = a_e + \frac{3}{2} (Z\alpha^2) + \alpha^2 \left( \log 2 - \frac{5}{2} \right) - \frac{8\alpha^3}{3\pi} \log \alpha (\log \alpha - \log 4 + \frac{281}{480}) + 18.984 \cdot \frac{\alpha^3}{\pi} + \dots, \quad (1.30)$$

where  $a_e$  is the electron anomalous magnetic moment.  $\delta^{QED}$  do not depend on the electron or proton masses, the corrections due to their masses are included in  $\delta^{struc}$ .

$\delta^{Zemach}$  was calculated by Zemach [18] and it takes into account both the charge and the magnetic moment of the proton; it can be written in the form [21]:

$$\delta^{Zemach} = -2Z\alpha\mu \langle r_{em} \rangle, \quad (1.31)$$

where  $R_p$  is the Zemach radius defined as:

$$\langle r_{em} \rangle = \int d\mathbf{r} r \int d\mathbf{r}' \rho(|\mathbf{r} - \mathbf{r}'|) \rho_{\text{mag}}(\mathbf{r}') \quad (1.32)$$

$$= -\frac{4}{\pi} \int_0^\infty \frac{dQ}{Q^2} \left( G_E(Q^2) \frac{G_M(Q^2)}{\mu_p} - 1 \right); \quad (1.33)$$

the (-1) term is necessary to avoid to double consider the proton charge and magnetic moment;  $\rho$  and  $\rho_{\text{mag}}$  are the the proton charge and magnetic densities.

By means of scattering experiments, as previously described, it is possible calculate the charge and magnetic form factors permitting to obtain the proton Zemach radius.

$\delta^{\text{recoil}}$  contains all the contributions of terms that depend on the ratio  $m_e/m_p$ .

$\delta^{\text{pol}}$  incorporates the corrections to the hyperfine splitting due to the fact that the charge and magnetic moment distributions are polarised by the orbiting electron; it does not exist a model independent to measure this correction by means of physical observable, it can be fixed an upper bound from theoretical calculations.

$\delta^{\text{hvp}}$  is related to the hadron vacuum polarization and, in particular, to the photon propagator in the Feynman diagrams that describe the lepton-proton interaction.

In table 1.1 the magnitude and the uncertainty of each correction for regular and muonic hydrogen are summarised.  $\delta^{\text{QED}}$  are of the same order except for the uncertainty that can be due to different vertices contribution in the muon-proton interaction.  $\delta^{\text{rigid}} = \delta^{\text{Zemach}} + \delta^{\text{recoil}}$  and also  $\delta^{\text{recoil}}$  are three order of magnitude larger in muonic hydrogen: this is reasonable since  $\delta^{\text{recoil}}$  includes the energy corrections due to the lepton-proton mass ratio.  $\delta^{\text{pol}}$  is found by subtracting the theoretical and the experimental hyperfine energy differences, also in this case for the muonic hydrogen the correction is three order of magnitude larger. The  $\delta^{\text{hvp}}$  does not give a considerable contribution to hydrogen whereas is of the same order of magnitude of the others corrections in muonic hydrogen.

The hyperfine energy splitting of hydrogen ground state is directly linked to the electromagnetic size of the nucleus by the relation found by Zemach [18]:

$$\Delta E_{\text{hyp}} = \frac{16}{3} \alpha^2 c R_\infty \left( \frac{\mu_2}{\mu_1} \right) \left( \frac{\mu_1}{\mu_1^0} \right)^2 \left( 1 + \frac{m_e}{m_p} \right)^{-3} \times \left[ 1 + \frac{3}{2} \alpha^2 - 2 \frac{\langle r \rangle_{em}}{a_0} + \beta + \delta \right], \quad (1.34)$$

where  $\mu_1^0$  is the Bohr magneton,  $m_e$  and  $m_p$  are the electron and proton masses,  $\left( 1 + \frac{m_e}{m_p} \right)^{-3}$  is the reduce mass correction due to the assumption of a Coulomb wave function at the origin. The last two terms ( $\beta$  and  $\delta$ ) are constants function of  $\alpha$ ,  $m_e$ ,  $m_p$  and of the total proton moment in nuclear magnetons.

Table 1.1: Summary of the magnitude and the uncertainty of each correction for regular and muonic hydrogen [20].

	Hydrogen		Muonic Hydrogen	
	magnitude	uncertainty	magnitude	uncertainty
$E^F$	1420 MHz	0.01 ppm	182.443 meV	0.1 ppm
$\delta^{QED}$	$1.16 \cdot 10^{-3}$	$<0.001 \cdot 10^{-6}$	$1.16 \cdot 10^{-3}$	$10^{-6}$
$\delta^{rigid}$	$39 \cdot 10^{-6}$	$2 \cdot 10^{-6}$	$7.5 \cdot 10^{-3}$	$0.1 \cdot 10^{-3}$
$\delta^{recoil}$	$6 \cdot 10^{-6}$	$10^{-8}$	$1.7 \cdot 10^{-3}$	$10^{-6}$
$\delta^{pol}$	$1.4 \cdot 10^{-6}$	$0.6 \cdot 10^{-6}$	$0.46 \cdot 10^{-3}$	$0.08 \cdot 10^{-3}$
$\delta^{hvp}$	$10^{-8}$	$10^{-9}$	$0.02 \cdot 10^{-3}$	$0.002 \cdot 10^{-3}$

The value of the proton Zemach radius  $\langle r_{em} \rangle$  is obtained by inserting all the constants and the experimental values of  $\Delta E$  and  $\mu_2/\mu_1$  in equation 1.34.

The calculation of the Zemach radius using e-p and  $\mu$ -p scattering and also spectroscopic techniques gives results that differ up to  $7 \sigma$ ; therefore, also in this case, there is a discrepancy between theory and experimental results. In these years some different hypotheses were proposed about the motivations of this disagreement: it can be ascribed to a wrong measurement of the physical constants, as the Rydberg one, or to the presence of new physics not completely described by QED.

### 1.3.2 Zemach radius results

The determination of the proton Zemach radius is important to clarify the *proton radius puzzle*; some experiments were proposed and they are on going as the one proposed by Japanese [22] and the one proposed by the CREMA collaboration [23]. Both of them aim to measure the hyperfine energy splitting of the muonic hydrogen.

The Japanese experiment apparatus is made up of three parts: a hydrogen gas target, a mid-infrared laser and a decay electrons detection system. The muons with momentum of 40 MeV/c are sent into the gas target where the form muonic hydrogen in an excite state ( $n \approx 14$ ); after the radiative cascade the  $\mu p$  is in the ground state in a singlet ( $F=0$ ) or triplet ( $F=1$ ) configuration. By means of a mid-infrared circularly polarised laser the  $\mu p$  are excited to the triplet configuration. The transition happens only if the laser energy corresponds to the hyperfine energy splitting of 0.183 eV. The polarised muons decay emitting electrons asymmetrically to the spin direction and they can be detected using the counters placed forward and backward the target. The decay asymmetry is the signal of the triplet to singlet transition. The gas is at low density to keep the muon polarisation.

The CREMA collaboration proposed to measure the HFS with a different technique: the experimental apparatus is made up of a hydrogen gas target in which a high Z wall is placed, a mid- infrared tunable laser and a X-rays detection

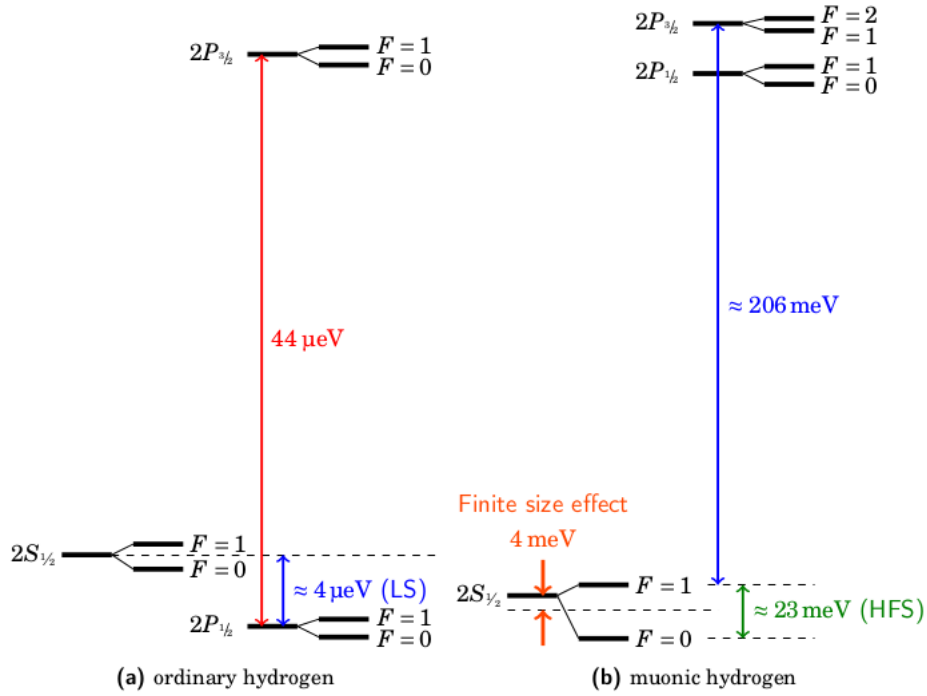


Figure 1.6: A graphic representation of electronic (a) and muonic hydrogen (b) levels [7]. The Lamb shift contribution is three orders of magnitude larger in regular hydrogen than in the muonic one.

system. The muons, with a  $10 \text{ MeV}/c$  momentum, are sent in the target forming muonic hydrogen. Also in this case a laser pulse set at the HFS frequency is sent in the target to induce the singlet-triplet transition. At this point the  $F=1$   $\mu\text{p}$  de-excites gaining kinetic energy. Exploiting the muon transfer rate to  $\mu\text{p}$  to the higher  $Z$  atom present in the internal wall,  $\mu Z$  atoms are created in an excited configuration; after the de-excitation X-rays with energy corresponding to the  $\mu Z$  atom transition are emitted and detected. Performing a scan over laser frequencies a resonance plot is obtained peaked at the HFS  $\mu\text{p}$  value.

These two methods are based on the singlet excitation by means of a tunable laser, however they differ in the way this laser is employed: the Japanese group exploits the polarisation on the muon whereas the CREMA collaboration exploits the muon transfer rate. These results, obtained with independent measurements, are necessary to better understand the *proton radius puzzle*.

### 1.3.3 Future perspectives: the FAMU experiment

In this context, the FAMU experiment will contribute to test the QED and to better understand the proton radius problem.

The aim of the FAMU experiment (Fisica degli Atomi MUonici - Muons Atom Physics) is the estimate of the proton Zemach radius by measuring the hyperfine energy splitting of the muonic hydrogen ground state. As it can be seen

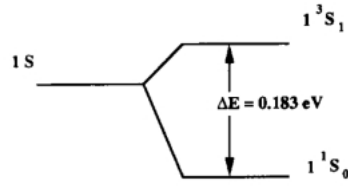


Figure 1.7: Muonic hydrogen ground state hyperfine splitting.

in figure 1.7 the muonic hydrogen ground state is divided in two levels with an energy difference of 0.183 eV. This measurement has never been done before and it represents the missing piece to complete the frame of the proton radius results. Furthermore FAMU will perform the measurement with an unprecedented statistics and precision.

The determination of the proton radius with a new technique is fundamental, not only to give another result to be compared with those found in different ways, but also to test the QED. This theory is very precise and it describes very accurately all the electromagnetic interactions; however, the discrepancy in the proton radius measurements could hide physics beyond the Standard model never observed before.

Moreover the FAMU measurements will permit to deeply study and analyse the transfer rate process, that is one of the central parts of the experimental method.

# Chapter 2

## FAMU experimental method

The determination of the proton Zemach radius with muonic atoms spectroscopy is motivated by the necessity to obtain an independent result that can either support previous results or can confirm the proton radius problem. The determination of the proton Zemach radius via a direct measure of the hyperfine splitting of the muonic hydrogen has never been done before so this measurement is a challenge both for the physical result and for the experimental techniques involved.

### 2.1 The FAMU concept

The aim of FAMU experiment is determination of the proton Zemach radius by directly measuring the hyperfine energy splitting ( $\Delta E^{hfs}$ ) of the muonic hydrogen ground state with a relative precision below 1% [24]. To reach the goal, the experiment combines particle physics concepts and atoms spectroscopic techniques. A conceptual scheme of the FAMU experimental method is shown in figure 2.1.

A muon beam is sent to a hydrogen gas target to form muonic hydrogen atoms: about the 25% are in a singlet configuration ( $F=0$ ) whereas about 75% is in the triplet ( $F=1$ ) one. Colliding with  $H_2$  molecules these muonic atoms thermalise and the  $\mu p^{F=1}$  de-excites into  $\mu p^{F=0}$ . At this point, almost all the  $\mu p$  are in the ground state in a singlet configuration. By means of a mid-infrared tunable laser, set at the HFS frequency, a series of singlet to triplet transitions are induced. Then the  $\mu p^{F=1}$  de-excites in collisions with  $H_2$ . The transition energy is partly converted in kinetic energy of the  $\mu p$ - $H_2$  system; in this way the  $\mu p$  gains about the two-thirds of the hyperfine transition energy ( $\approx 120$  meV) [25].

The hyperfine transition energy is of the order of hundreds meV and it is too small to be detected directly. To solve this problem, FAMU exploits the muon transfer rate to higher Z gases. The  $\mu p$  with higher kinetic energy transfers the muon to the heavier atom present in the mixture. The muon occupies an excited state of the Z atom and immediately after it de-excites to the ground state emitting characteristic X-rays. The emitted radiation has an energy of the order of keV and can be detected directly.

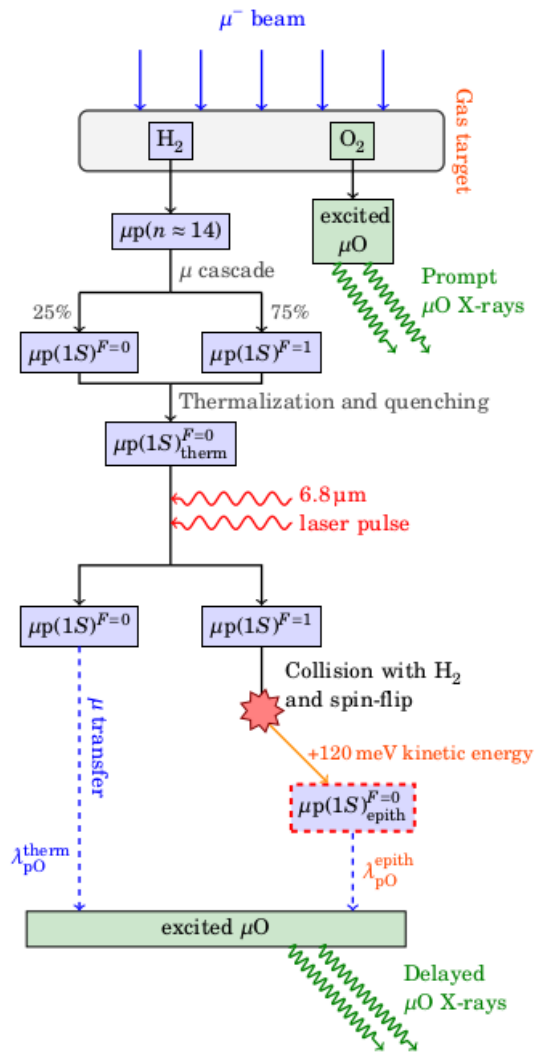


Figure 2.1: FAMU experimental method conceptual scheme [7].

Performing a scan over the laser frequencies near to the energy of the muonic hydrogen hyperfine transition, and counting the number of events as function of laser energy a resonance plot is obtained, peaked at HFS energy.

In order to maintain the laser radiation inside the gas for more time before its natural degradation and to increase the interaction probability, a multipass cavity is placed inside the target.

## 2.2 Prompt phase: muonic atom formation and thermalisation

Muonic atoms are created in a gas target containing hydrogen with a small contamination of another higher  $Z$  gas. Muons enter in the target and, after colliding with the gas molecules, they are slowed down. This low energy muons can undergo atomic capture due to the Coulomb field of the nucleus, forming  $\mu\text{p}$  systems or  $\text{pp}\mu$  molecules. The muon is captured in an external orbit,  $n \sim 14$ , and in about 1 ns it de-excites in an atomic cascade to  $n \approx 5$  emitting an Auger electron or it can be captured with the immediate expulsion of an electron. In the transition to the ground state, the atom emits radiation with energy of about 2 keV, that can not be detect directly. Due to the interaction between muon and proton spins, the ground state can be in a singlet ( $F=0$ ) or triplet ( $F=1$ ) configuration with a statistical weight of about 1:3 respectively; after the  $\mu\text{p}$  de-excitation the ground state acquires kinetic energy with maximum values near keV. The collisions between  $\mu\text{p}$  and  $H_2$  and other high  $Z$  molecules causes the  $\mu\text{p}$  thermalization and spin-flip.

Monte Carlo studies show that the thermalisation process depends on the hydrogen density  $\phi$ . These studies were performed considering a gas composition of  $H_2 + O_2$ : in figure 2.2 the time evolution of the  $\mu\text{p}$  energy is shown as function of different temperatures at fixed  $\phi$ . The  $\mu\text{p}$  thermalised after about 150 ns independently on the temperature; for times smaller than 150 ns the curves difference is due to the different thermal energy of the  $H_2$  molecules.

The triplet state de-excitation after colliding with gas molecules involves the triple state depopulation that is faster than the thermalisation process. In figure 2.3 the time evolution of the triplet state population is shown; each curve is obtained at fixed temperature with different gas pressures. Comparing this result to the one found for the energy time evolution for  $\mu\text{p}$  in the same conditions of pressure and temperature, reported in figure 2.4, it can be noticed that the de-population time is ten time lower.

Taking into account both thermalisation and depopulation the time  $t_0$  at which the system can be considered thermalised is [26]:

$$t_0 \sim 20 \times \frac{T}{P} \frac{[\text{K}]}{[\text{atm}]}. \quad (2.1)$$

The collision of the  $\mu\text{p}$  with  $H_2$  molecules causes the formation of  $\text{pp}\mu$  molecules; also in this case the  $\text{pp}\mu$  formation rate is different for the singlet ( $\lambda_{of}$ )

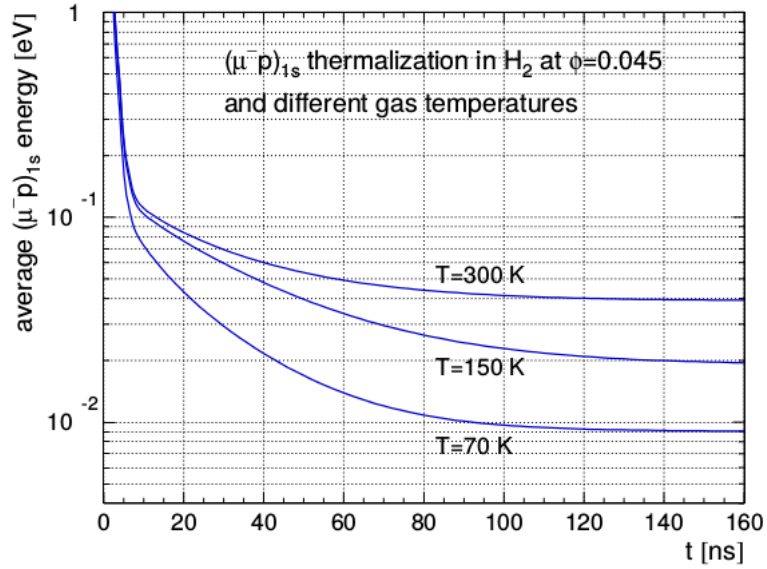


Figure 2.2: Time distribution of the  $\mu p$  energy in the ground state: after 150 ns the system is thermalised independently on the temperature [26].

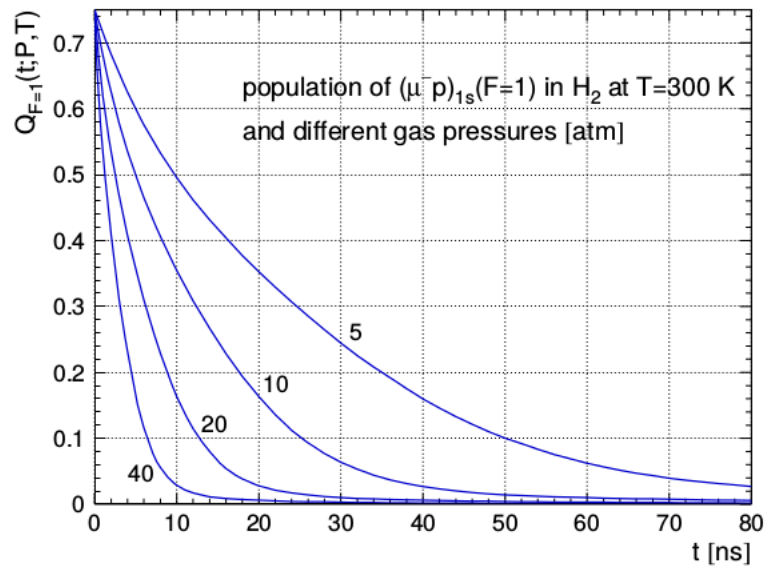


Figure 2.3: Time distribution of the  $\mu p$  population in a triplet state ( $F=1$ ) for different gas pressures. The  $F=1$  de-population process is faster, about 80 ns, than the thermalisation one [26].

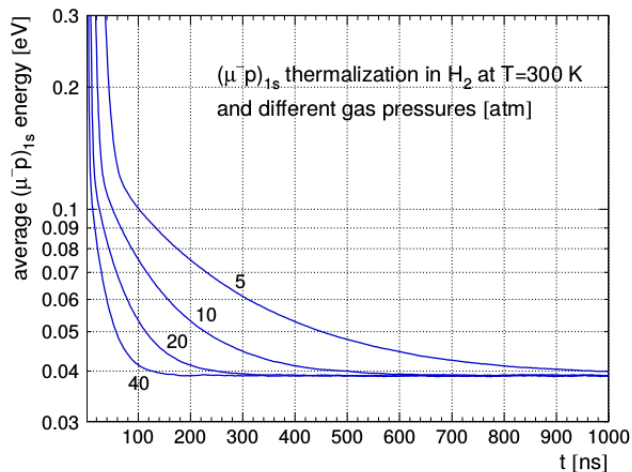


Figure 2.4: Time distribution of the  $\mu p$  energy in the ground state for different pressure values at fixed temperature: the thermalisation process is faster for higher pressures [26].

or for the triplet configuration ( $\lambda_{pf}$ ). The total  $pp\mu$  formation rate is the sum of the two,  $\lambda_{pp\mu} = \lambda_{of} + \lambda_{pf}$ . The effective formation rate measured in experiments is:

$$\Lambda_{pp\mu} = \phi \lambda_{pp\mu}, \quad (2.2)$$

it scales with hydrogen density. In FAMU  $\phi$  is constant so the  $pp\mu$  contribution is constant.

The natural abundance of deuterium in hydrogen can cause the formation of  $\mu d$  atoms and  $p\mu d$  molecules in the target. The  $\mu d$  formation rate is temperature dependent [27]. If the muon is captured to form  $\mu d$  or  $pp\mu$  molecules it is not transferred to the  $Z$  atom and it can be considered lost.

Muons can decay in electrons and neutrinos; electrons interact electromagnetically with the gas molecules emitting *bremstrahlung* radiation. This radiation produces a background spread in all the energy spectrum.

When muons interact with the atomic nucleus, they can undergo nuclear capture:  $\mu + p \rightarrow n + \nu$ ; this interaction does not produce background but changes the nature of the gas composition. Muons nuclear capture is three order of magnitude smaller than the muon decay, so it can be neglected [28].

At the end of the prompt phase, the gas is thermalised and the  $\mu p$  are in the singlet configuration in the ground state.

## 2.3 Delayed phase: laser excitation and hyperfine splitting measurement

At this point, a mid-infrared laser set in a frequency range centered at the theoretical value of the hyperfine splitting of the muonic hydrogen is sent to the target. The muonic hydrogen absorbs the incoming photons making a singlet to triplet transition; colliding with  $H_2$  molecules it de-excites to the singlet configuration

gaining about 0.12 eV kinetic energy. Since the singlet to triplet transition energy is too small to be detected directly, the method proposed is to evaluate the number of muons that spin-flip after the laser pulse exploiting a relation whose rate depends on the  $\mu p$  energy. It was found that the transfer rate of the muon from  $\mu p$  to higher  $Z$  atoms, as oxygen, depends on the  $\mu p$  energy at epithermal energies. The muon transfer process can be schematised as:



The idea to exploit this property was first proposed by Bakalov and collaborators [29]: in their purpose, the target was filled with  $H_2$  with inside some thin foils of gold. After the  $\mu p$  formation, some  $\mu p$  reach the gold surface and transfer their muon according to:



The time distribution of the X-rays emitted from gold without the laser pulse should exhibit a decreasing exponential behaviour; if a laser pulse with frequency in the muonic hydrogen hyperfine splitting is sent the number of singlet to triplet transition is increased, the  $\mu p$  acquired a larger kinetic energy and the number of muons transferred from  $\mu p$  to gold is increased sharing a peak in the events time distribution. The laser frequency at which the difference of the two curves is larger corresponds to the hyperfine energy.

The major problem of this configuration was to efficiently illuminate the gas target. This method was improved substituting the gold foils with a higher  $Z$  gas contamination in the  $H_2$  gas. In this way the cavity can be placed inside the target increasing the number of transferred events.

In FAMU the properties of the muon transfer rate to higher  $Z$  gases are exploited to determine the number of muonic hydrogen atoms that spin-flip after the laser excitation.

## 2.4 Transfer rate measurement

To determine the transfer rate as function of  $\mu p$  energy, the proposed method evaluates the transfer rate after a time  $t > t_0$  ( $t_0$  is the time at which the system can be considered thermalised); even though the transfer rate is three times larger at epithermal energies than at the thermalised ones, the study of the muon transfer rate is performed in a thermalised condition in order to have the temperature and, as consequence, the energy of the system under control. If the system is thermalised the energy distribution can be parametrised with a Maxwell-Boltzmann function in which the temperature value is equal to the target temperature.

After the triplet state de-excitation the  $\mu p$  acquires kinetic energy. Thanks to the energy dependence of the transfer rate, the  $\mu p$  with increased kinetic energy will transfer its  $\mu$  to the  $Z$  atom present in the gas mixture faster than before the laser excitation. A theoretical study of the energy dependence of the transfer

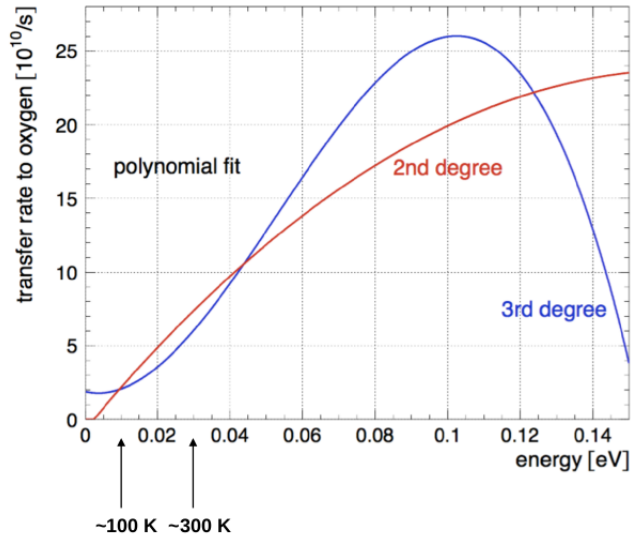


Figure 2.5: Transfer rate dependence on  $\mu p$  energy for two different trends assumptions, in red a second degree polynomial and in blue a third degree polynomial [30].

rate from  $\mu p$  to oxygen is performed and it is shown in figure 2.5: from the experimental results the transfer rate dependence is extrapolated assuming two different behaviours, described with polynomials of second and third order. In both cases  $\mu p$  with higher kinetic energy have a higher transfer rate.

The transferred muon is captured in an external orbit of the  $Z$  atom; the new mesic atom de-excites emitting characteristic X-ray with energies that depend on the levels transitions.

The X-rays emitted by a  $\mu Z$  atom are due to the atomic muon capture and to the muon transfer from  $\mu p$  to the  $Z$  atom; if the X-ray emission is a consequence of the muon transfer from the muonic hydrogen ground state they appear delayed respect to the muons stop in the target.

There are some physical parameters that can be adjusted to obtain the best experimental conditions to study the transfer rate such as: the target temperature and pressure, the gas composition and concentration. One of the most studied gas that shows a transfer rate energy dependence is oxygen.

To determine the best physical conditions to study the transfer rate dependence on the  $\mu p$  energy some Monte Carlo simulations were realised considering a gas mixture of hydrogen and oxygen [26]. In figure 2.6 the time evolution of the  $\mu p$  population at fixed temperature and pressure is shown; the different curves correspond to different gas concentrations. The  $\mu p$  population disappears at a faster rate when increasing the oxygen concentration. At a concentration of 1% it disappears in a time that is of the same order of magnitude of the thermalisation one. The best oxygen concentration is the one that assures the maximum number of muon transferred events from thermalised  $\mu p$  to oxygen.

In figure 2.7 the number of muon transferred events, normalised for the number of muons stopped in the gas, as function of oxygen concentrations at fixed values

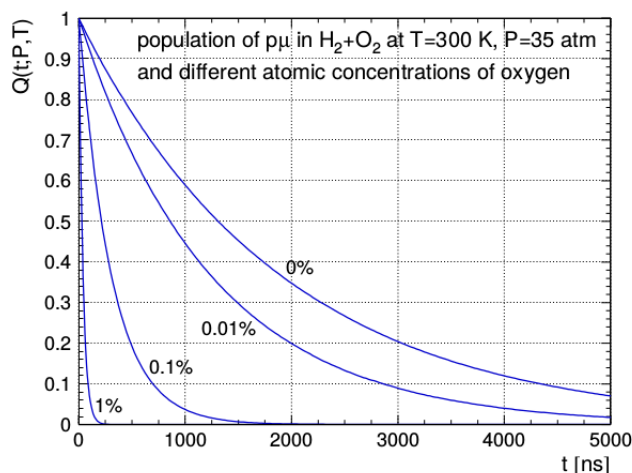


Figure 2.6: Time evolution of the  $\mu p$  population at fixed temperature and pressure; the different curves correspond to different gas concentrations [26].

of temperature and pressure ( $T=300$  K,  $P=35$  atm) is shown. This curve is useful to determine the oxygen concentration to reduce the statistical error, that is inversely proportional to the square root of the number of transferred event, on the transfer rate measurement.

The hypothesis of a transfer rate energy dependency requires the knowledge of the time evolution of the  $\mu p$  atom energy distribution. In the procedure to determine the number of muons transferred from  $\mu p$  to the higher  $Z$  atom as function of time, several delayed energy spectra based on different time windows are analysed. These energy spectra are originated by the  $Z$  atom X-rays emission after de-excitation: for each time interval the intensities of the spectrum peaks are analysed. The time distribution of X-rays intensities shares a single exponential structure; the fit parameter is the muon transfer rate to the  $Z$  atom and, since the time selection includes only thermalised  $\mu p$ , the fit parameter is the mean transfer rate from thermalised  $\mu p$  to  $Z$  atom.

The exponential parameter of the fit function can also be interpreted as the mean lifetime of the muonic hydrogen at the ground state.

To determine the curve that describes the transfer rate as function of the energy is fundamental to perform the final measurement in the best experimental conditions. Infact the final measurement will be performed at fixed temperature and pressure and with a specific concentration of a  $Z$  gas in order to have the maximum transfer rate at the energy of the hyperfine splitting of muonic ground state.

The final measurement procedure is based on two phases repeated several times: in the first phase the muon beam is sent to the target where there is the formation of  $\mu p$  atoms; they transfer the muon to the  $Z$  gas which de-excites emitting characteristic X-rays. The time distribution of these intensities is recorded. In the second phase, after the  $\mu p$  thermalisation, a laser pulse is sent to the target inducing the singlet to triplet transitions. If the laser energy is correct,

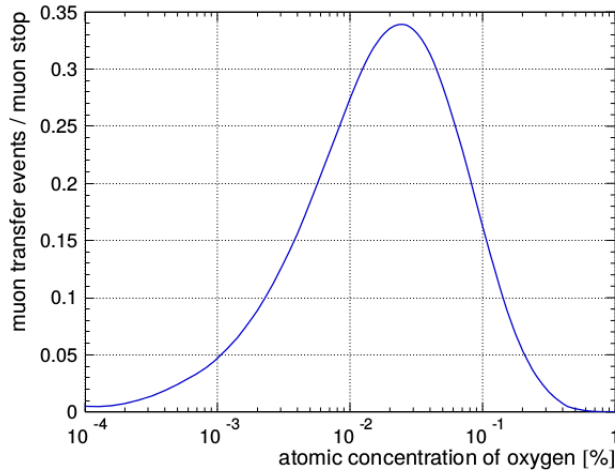


Figure 2.7: Number of muon transfer events, normalised for the number of muons stopped in the gas, as function of oxygen concentrations at fixed values of temperature (300 K) and pressure (35 atm) [26].

the number of transferred events is larger respect to the result obtained without laser: this results in a peak in the time distribution of the number of events. An example of the result of these two phases is obtained by means of a simulation that is shown in figure 2.8. The black line represents the single exponential behaviour resulting from the muon transfer without the laser. The blue and red lines are obtained with the same laser energy but with two different dimensions of the cavity. When a laser pulse is sent into the target, a peak appears in the time distribution. The frequency corresponding to the hyperfine transition is the one that generates the maximum difference between the two curves. Subtracting the two curves it is possible to obtain the integral of the number of events as function of the laser frequency. Repeating this procedure for different laser frequencies close to the theoretical value of the hyperfine splitting, the result is a resonance plot centered at the hyperfine energy value: an example is shown in figure 2.9. The plot is the result obtained by Pohl and collaborators for the measurement of the proton charge radius; however the shape of the curve should be the same also for the hyperfine splitting measurement. Substituting this frequency in the formula described in section 1.3 the Zemach radius can be calculated.

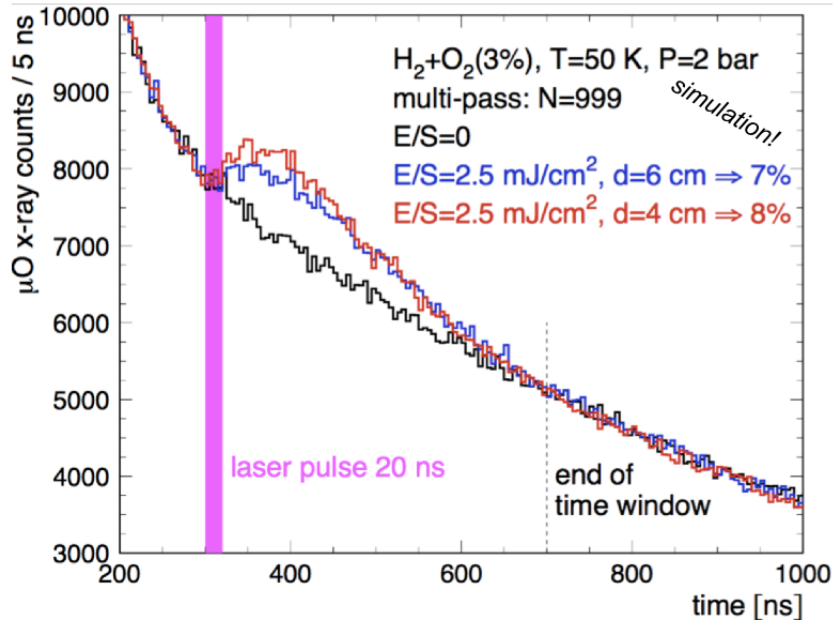


Figure 2.8: Simulation result of the time distribution of the delayed X-rays emission: black line without laser excitation, blue and red lines with laser excitation [30].

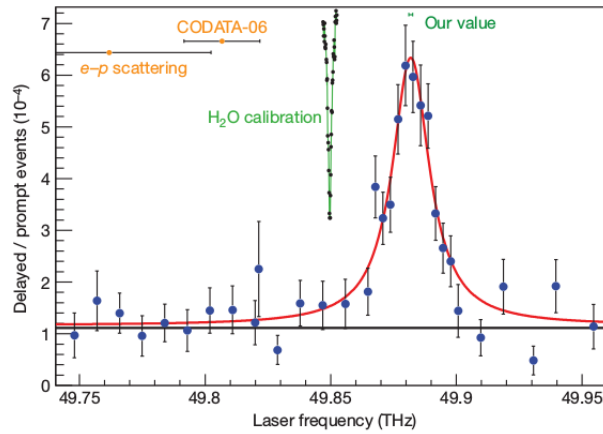


Figure 2.9: Resonance plot obtained by Pohl and collaborators for the determination of the proton charge radius [4]. The filled blue circles are the number of events in the laser time window normalised to the number of prompt events as a function of the laser frequency. The CODATA and e-p scattering results are indicated in orange; the red line is the fit function.

# Chapter 3

## Experimental apparatus

The FAMU experiment started in 2014 with very preliminary measurements to test the feasibility of the measure: the control of the muon beam and of the detection system; the data acquisition and analysis. For these measurements a first target in aluminium was realised.

For the 2016 acquisition a new target was build, in aluminium alloy with an internal coating; this target was cryogenic and pressurised and it was optimised for the transfer rate measurement.

A third target with the optical cavity placed inside will be produce for the final measurement combined with the installation of the laser system. Also this target will be cryogenic and pressurised.

The 2016 FAMU experimental apparatus is made up of a central gas target, around which detectors are placed. In the upper part, a cooling head controls the target temperature. An electronic system for data acquisition and control is used together with an online data processing and storage. The beam is made up of negative muons. This apparatus is devoted to the transfer rate measurement, the laser and the optical cavity are not installed.

In this chapter I will describe all the components of the FAMU apparatus, giving large space to the parts relevant for a better understanding of the analysis results.

### 3.1 Muon beam

To create the muonic atoms the experiment exploits a muon beam produced at the ISIS complex of accelerators at Rutherford Appleton Laboratory (RAL) [31], located on the Harwell Science and Innovation Campus in Oxfordshire. The experiment is installed at RIKEN-RAL muon facility [32], that is one of the structures connected to ISIS synchrotron.

To produce muons the synchrotron accelerates protons up to 800 MeV; protons are then sent to a carbon target that, after the protons interaction, emits neutrinos and pions. Pions are unstable particles that decay in muons. Muons are then accelerated and delivered to the four experimental ports at the RIKEN-RAL

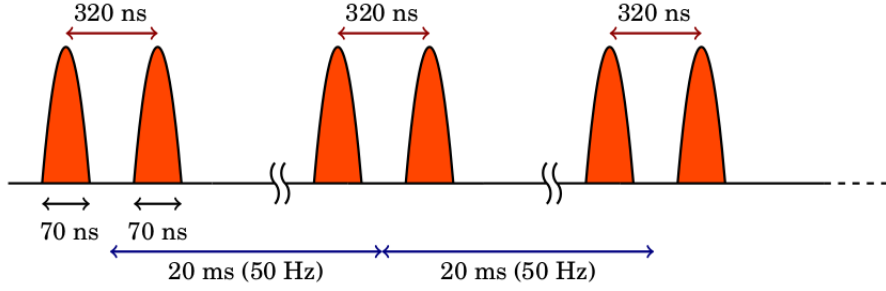


Figure 3.1: Graphic representation of the double pulse muon beam [7].

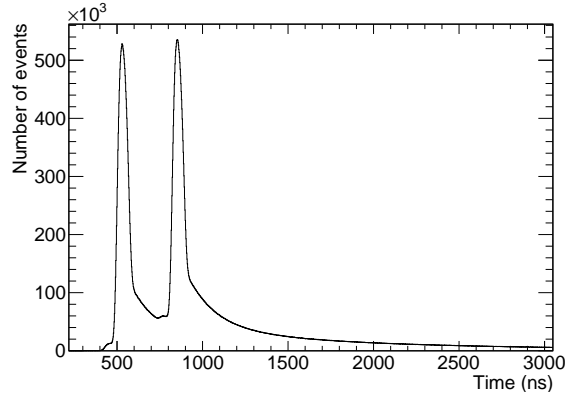


Figure 3.2: Time spectrum acquired with Lanthanum Bromide scintillators: the double pulse of the beam is reflected in the data

facility.

The main characteristics of the beam are the high intensity, about  $10^5 \text{ s}^{-1} \text{ cm}^{-2}$ , and the time shape, a double pulse with a frequency of 50 Hz. Each pulse is 70 ns long and the delay between the two pulses is about 320 ns, as it is represented in figure 3.1. The starting muon momentum has a gaussian distribution with  $\sigma_E/E \approx 10\%$  [33].

The muon beam double pulse structure is reflected in the data time spectrum. When muons enter the target they can be captured by the gas atoms that, after the de-excitation, emit X-rays. This radiation is revealed by the detectors that produce a signal. Therefore the muons time arrival distribution is proportional to the detected X-rays time distribution that can be seen in figure 3.2. It has two spills corresponding to the two muon pulses.

## 3.2 Gas target

The target is made up of two coaxial cylinders and it was produced by Criotec Impianti S.R.L. [34] using the aluminium alloy Al6061. This alloy is made up aluminium for the large part ( $\sim 98\%$ ) and of some other metals as Si, Fe, Mg and

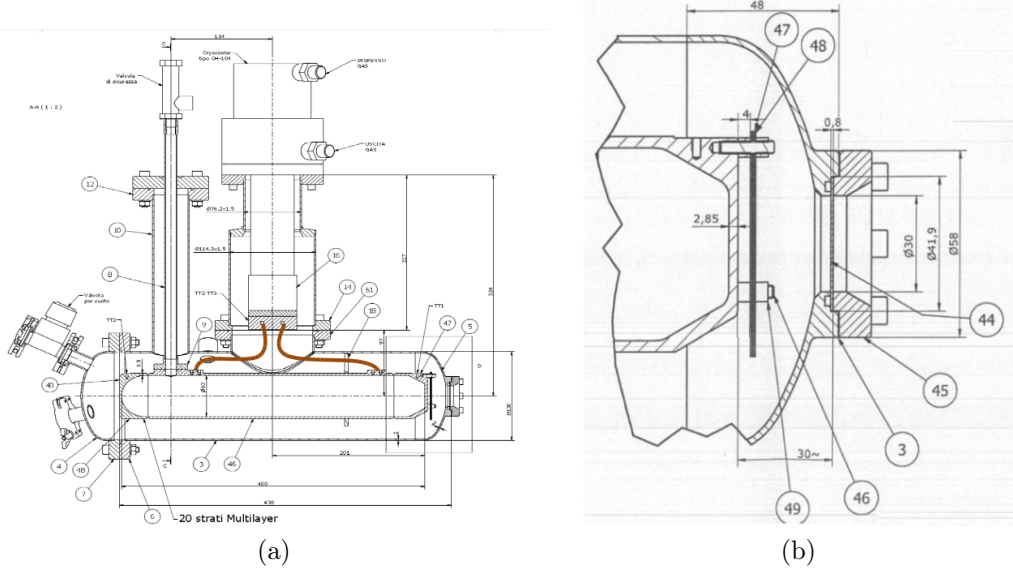


Figure 3.3: The target lateral section and a focus on the entrance window section are shown in figure (a) and (b) respectively.

Cr. This is employed because of its high resistance to corrosion, good mechanical properties and strength. The target is pressurised and cryogenic to maintain the gas at constant temperature during the acquisition.

The external cylinder has a diameter of 132 mm diameter and is about 500 mm long. The thickness of the walls is 2 mm, except for a circular entrance window of 30 mm diameter thinned to 0.8 mm.

The internal cylinder is made up of aluminium with a double coating of gold and nickel. It is 406 mm long with an internal diameter of 60 mm. The thickness of the walls is 3.5 mm, whereas the entrance window is 2.85 mm thick. It is enveloped in a multilayer insulator and, to reach the best temperature stability, it was separated from the outer cylinder by vacuum. In figure 3.3(a) is shown a target section with the dimensions of the different parts. In figure 3.3(b) is displayed the target front part zoomed on the entrance window: the layer indicated with the number 47 is the thin entrance window thermal shielded with three aluminium foils, separated by plastic plates, with thickness between 70 and 75  $\mu\text{m}$  each. These characteristics ensure a certified resistance to gas pressure of several tenth of bar, a thermal isolation and target stabilisation for temperature from 35 K to 323 K. The entrance window is designed to minimise the number of muons that stop at the interface and to reduce the multiple scattering.

The internal coating of gold and nickel is necessary to reduce the background electrons produced by muon decay.

Muons are unstable particles with mean life time of about 2.2  $\mu\text{s}$  in vacuum [35]. When bounded to a nucleus they can decay,  $\mu^- \rightarrow e^- \bar{\nu}_e \nu_\mu$ , or undergo nuclear capture,  $(A, Z) + \mu^-(1S) \rightarrow (A^*, Z - 1) + \nu_\mu$ .

If muons decay, they generate background electrons that are detected and increase the energy spectrum background. From experimental measurements a

dependence of the muon mean life time for nuclear capture as function of the nucleus  $Z$  was seen [36]. In figure 3.4(a) the dependence of the number of remaining muons as function of time when they interact with different elements is shown. In particular, the higher the nucleus  $Z$ , the greater is the number of captured muons as function on time. To reduce the electrons background problem, the FAMU experiment exploited the nuclear capture. The inner coating of the target was made of gold and nickel to capture muons that arrived to the target walls reducing their decay probability in the delayed phase. The muon stop in aluminium has to be avoided because, since the mean lifetime of  $\mu\text{Al}$  is close to  $\mu\text{O}$ , the aluminium produces background in a temporal region where the oxygen signal is.

Hence, the beam momentum is tuned to have the muons Bragg peak centered in the gas and to minimise the stop in the aluminium. In figure 3.4(b), obtained from simulation, the fraction of muon stopped in the different elements of the target is shown as function of muon momentum: if the muon momentum is in the [55, 60] MeV/c interval, the number of muons stopped in nickel, gold and gas reaches the maximum whereas those that stop in the aluminium target walls are drastically reduced. For the 2016 data acquisition the beam momentum was 57 MeV/c. This value was fixed after a scan over the momentum values resulting from the simulation and considering the 2014 analysis and the simulation results.

The target is filled with high pressure gas, at about 40 atm. In 2016 the measurements were performed with different gas mixtures at different concentrations:  $H_2 + Ar$  and  $H_2 + O_2$  at 1%, 0.05% and 0.3%,  $H_2 + CH_4$  and  $H_2 + CO_2$  at 0.3%. All the concentrations are measured by weight. The gas chosen for this analysis is the mixture of  $H_2$  with a 0.3% measured by weight of  $O_2$  because the data acquired with this concentration is the one with the largest statistics. This analysis will be performed also for the others gas mixtures.

A lead collimator with 3 cm diameter is placed between the target and the beam pipe.

## 3.3 Detectors

To obtain the transfer rate, the energy spectra evolution as function of time has to be studied. So, a X-rays detection system with excellent energy resolution and fast timing response is suitable for the the transfer rate measurement. In FAMU two types of X-rays detectors employed: LaBr3(Ce) scintillators and High Purity Germanium detectors (HPGe). The muon beam is monitored using a hodoscope, placed between the lead collimator and the gas target.

### 3.3.1 Lanthanum Bromide Scintillators

The LaBr3(Ce) detectors are latest generation inorganic scintillators.

A scintillator is a material that emits light in the visible band after the passage of radiation through its volume. The incoming radiation excites the scintillator

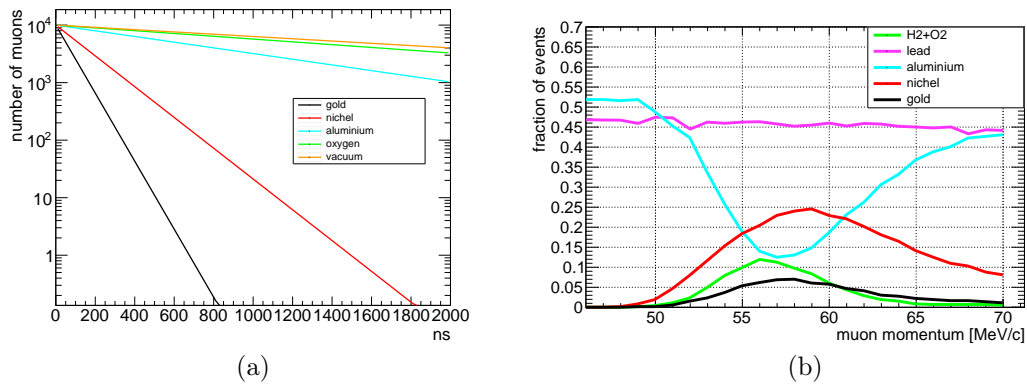


Figure 3.4: (a) Number of remaining muons as function of time in gold ( $Z=79$ , black), nickel ( $Z=28$ , red), aluminium ( $Z=13$ , cyan), oxygen ( $Z=8$ , green) and in vacuum (orange); plot realised using theoretical data. (b) Fraction of events stopped in the gas and in the target elements as function of the muon momentum ( $T=300$  K).

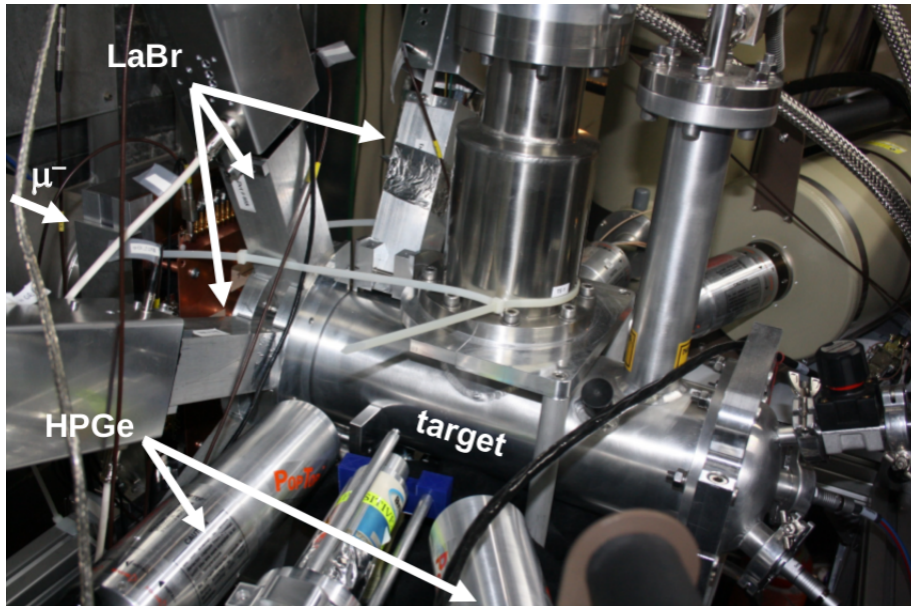


Figure 3.5: Picture of FAMU apparatus; from the left the beam pipe, the hodoscope, the LaBr<sub>3</sub>(Ce) crown and the HPGe detectors.

energy levels that, after de-excitation, emit light; the quantity of the emitted light is proportional to the energy released in the scintillator active volume. Each scintillator has to be coupled to a photomultiplier (PMT) which transforms the incoming light into a measurable analog signal.

In FAMU there are eight LaBr3(Ce) provided by INFN section of Bologna [37], arranged in a crown placed in the front part of the target as it can be seen in figure 3.5. Each LaBr3(Ce) crystal is 1 inch  $\times$  1 inch (diameter  $\times$  thickness) coupled with a compact PMT Hamamatsu R11265-200 [38]. They are characterised by fast timing response, excellent linearity and energy resolution [39]. A typical LaBr3(Ce) signal has rise time of about 10 ns and decay time of about 100 ns. The signal shape properties permit to reduce significantly the number of pile up events even in a high rate environment, as it is in FAMU.

The energy resolution is about 7.5% FWHM (Full Width at Half Maximum) at 12 keV and about 4% FWHM at 662 keV; this efficiency resolution is between those measured with other scintillators and with solid state detectors [39].

The LaBr3(Ce) scintillators have an intrinsic radioactivity due to the presence of  $^{138}\text{La}$  isotope. In the 66.4% of cases, the  $^{138}\text{La}$  decay undergoes via electronic capture in a  $^{138}\text{Ba}$  excite state. The  $^{138}\text{Ba}$  de-excite emitting 35 keV X-ray. The remaining 33.6% of  $^{138}\text{La}$  decays via  $\beta^-$  emission to an excite state of  $^{138}\text{Ce}$  that de-excite emitting 789 keV  $\gamma$  ray [40]. However, the number of background events respect to the total number of counts is negligible.

The fast time response combined with a great energy resolution make the LaBr3(Ce) scintillators suitable for the FAMU purpose.

### 3.3.2 High Purity Germanium detectors

The HPGes are solid detectors whose working principle is based on semiconductor properties and p-n junction.

Semiconductor materials have an energy band structure in which the valence band is completely occupied and the conduction band is empty. The energy difference between these two bands is called *energy gap* and it describes a forbidden region in which there are no electronic sites. The energy gap is of the order of the thermal energy at room temperature that is about 0.7 eV for Ge [41]. Therefore some electrons are excited in the conduction band leaving a hole in the corresponding valence band. When an electric field is applied, a current can be measured.

To increase the number of charge carriers (both electrons and holes), a semiconductor crystal is doped with other elements; in this way localised electronic states are generated under the conduction band (acceptor levels) and above the valence one (donor levels), and very close to them. Electrons from valence band are thermally excited to the acceptor levels leaving holes in the valence band, and electrons from donor levels are promoted to the conduction band increasing the conductivity of the material.

If the donors are prevalent, the material is said to be n-type otherwise, if the acceptor sites prevailing, the material is said p-type.

A p-n junction is a semiconductor device where a p-type region is in contact with a n-type region. At the interface between these two regions, charge carriers recombine until an electric field is created stopping the electrons and holes flux and the recombination. Therefore a depletion region is created at the interface where charge carriers are not present. Applying a potential difference (V) between the two regions, the depletion depth (d) is enlarged, as it can be inferred from equation 3.1:

$$d = \left( \frac{2\epsilon V}{eN} \right)^{1/2}, \quad (3.1)$$

where  $\epsilon$  is the dielectric constant,  $e$  is the electric charge, and  $N$  is the net impurity in the bulk semiconductor material [41].

When the incoming radiation passes through the active depleted volume creates a couple electron-hole that migrates following the electric field lines generating a signal.

To measure the energy of high penetrating radiation, the depletion depth has to be larger than 2 or 3 mm; even increasing the applied voltage to breakdown values the depth is not large enough to stop X-rays of hundreds of keV. In order to increase the depletion depth keeping the detector size reasonable, the only parameter that can be modified is  $N$ , the number of impurities.

The High Purity Ge detectors are treated to have an impurity concentration less  $10^{10}$  atoms/cm<sup>3</sup> (a usual  $N$  for silicon at room temperature is in the range  $10^{13} - 10^{18}$  atoms/cm<sup>3</sup>), obtaining a depletion depth of about 10 mm at 1000 V.

Since the energy gap of the forbidden region is of the order of thermal energy at room temperature, the HPGe have to be cooled to maintain their energy resolution. Each HPGe is provided with a dewar usually filled with liquid nitrogen to keep the temperature around  $\approx 77$  K. However, differently from the others solid state detectors, HPGe can be allowed to room temperature between uses.

The signal generated by the particle passage is not high enough to be directly recorded by the electronic acquisition system, so the first stage is the pre-amplification of the signal. A typical pre-amplified signal is represented in figure 3.6. The second stage is the amplification with a precise shaping time that is user defined and that determines the shape and the rise time of the amplified output signal.

The HPGe detectors are largely used in spectroscopy measurement because of their highest energy resolution among the solid state detectors, about 1 keV FWHM at 122 keV. Up to now the FAMU HPGe data were used to obtain a benchmark spectrum to precisely determine the composition of the target gas mixture.

In my analysis I used the data acquired with HPGe to perform a counting measurement as function of time; this analysis is challenging because the shaping time of amplified signal requires a particular care in time determination and correction, as it is discussed in chapter 4.

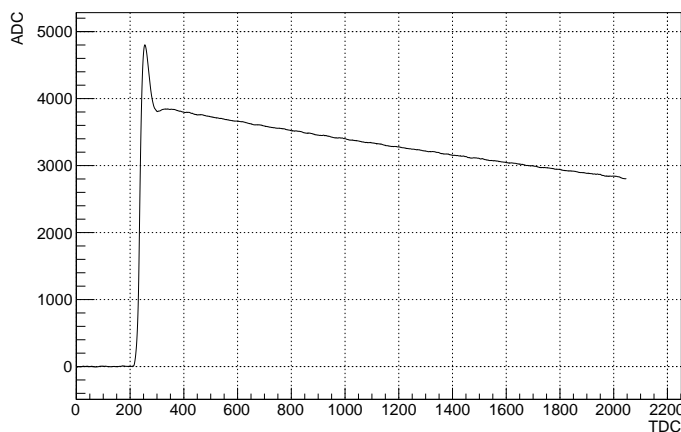


Figure 3.6: Example of a pre-amplified signal. The decay tail is very long (about  $10 \mu\text{s}$ ).

In FAMU there are four HPGe detectors placed beyond the LaBr<sub>3</sub>(Ce) crown: one ORTEC GLP (planar configuration) provided by INFN section of Milano Bicocca, two ORTEC GEM-S (semi-planar configuration), one provided by INFN section of Milano Bicocca and the other by RIKEN-RAL; the last is an ORTEC GMX Gamma-X (coaxial configuration) that is made available from RIKEN-RAL staff.

The ORTEC GLP is a low energy detector with an excellent energy resolution in 3 to 300 keV energy range (about 1% at 100 keV). The planar configuration is suitable for low energy X-rays detection: the electrical contacts are placed on the two flat surfaces of the germanium disk. The p contact can be produced using the ion implantation technique: this layer is very thin making it suitable as entrance window for weakly penetrating radiation. The ORTEC GLP installed in FAMU has 11 mm diameter and 10 mm thickness; it is isolated from the external environment by a  $127 \mu\text{m}$  berillium window. For ORTEC GLP the output of pre-amplifier and of the amplifier are acquired.

The ORTEC GMX Gamma-X is a coaxial germanium detector. The coaxial configuration is made up of a long germanium crystal with an inner cavity as long as the crystal length. The two electric contacts are on the outer and inner crystal surfaces. With this configuration, changing the dimension parameters as the length and the diameters, larger active volumes can be obtained making possible the measurements of higher energies. The HPGe ORTEC GMX Gamma-X is a n-type high-purity germanium photon spectrometer to use in applications over the energy range from 5 keV to 3 MeV. The carbon entrance window is  $0.9 \mu\text{m}$  thick, with 49 mm active diameter and 57 mm active depth. Only the amplified signal is acquired.

The remaining ORTEC GEM-S are the best compromise between the planar and coaxial configurations, both in terms of efficiency at low energy and energy reconstruction in the low medium range. The crystal dimensions are: diameter 30.4 mm, length 20.8 mm, inner cavity diameter 8.4 mm, cavity depth 10 mm.

Table 3.1: Summary of the calibration sources energies.

	keV	keV	keV
$^{57}\text{Co}$	122.06	136.47	14.41
$^{241}\text{Am}$	59.54		
$^{90}\text{Sr}$	545.9		
$^{137}\text{Cs}$	662.66		

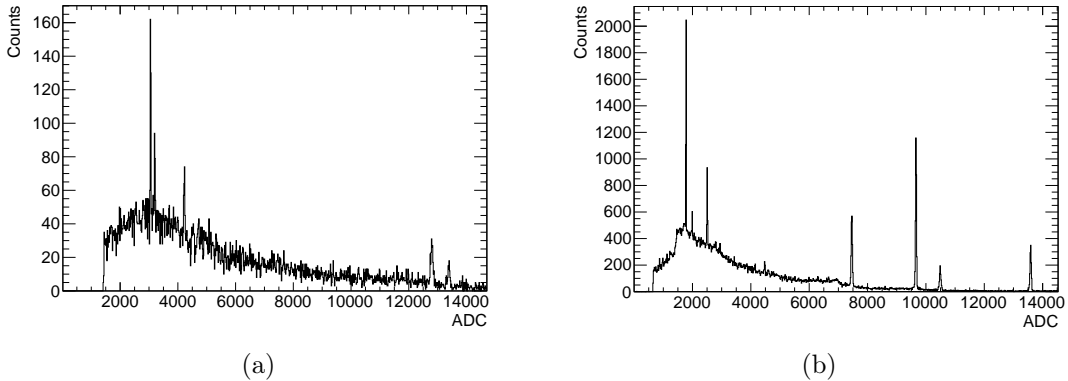


Figure 3.7: (a) ADC spectrum for the  $^{57}\text{Co}$  source; (b) ADC spectrum for the triple source of  $^{241}\text{Am}$ ,  $^{90}\text{Sr}$  and  $^{137}\text{Cs}$ .

For the Milan ORTEC GEM-S the output of the pre-amplifier, the amplifier and fast amplifier are recorded whereas for the RIKEN ORTEC GEM-S only the amplified output is saved.

Each detector is calibrated using  $^{57}\text{Co}$  and a triple source containing  $^{241}\text{Am}$ ,  $^{90}\text{Sr}$  and  $^{137}\text{Cs}$ .  $^{57}\text{Co}$  decays via nuclear capture in an excited level of  $^{57}\text{Fe}$  that de-excites via  $\gamma$  emission with energies (in order of branching ratio): 122.06 keV (85.49%), 136.47 keV (10.71%) and 14.41 keV (9.18%).  $^{241}\text{Am}$  undergoes  $\alpha$  decay in  $^{237}\text{Np}$  with a  $\gamma$  emission at 59.54 keV.  $^{90}\text{Sr}$  decays via  $\beta^-$  emission with a  $Q_{\beta^-}^2 = 545.9$  keV;  $^{137}\text{Cs}$  decays by  $\beta^-$  emission in an  $^{137}\text{Ba}$  excited state.  $^{137}\text{Ba}$  de-excites emitting  $\gamma$  ray at 662.66 keV with 89.99% probability. The energy values used to calibrate the data are summarised in table 3.1.

In figure 3.7 the cobalt and the triple source calibration spectra are shown; these spectra are acquired with the FAMU HPGe fast shaped. The energy peaks are narrow because of the high energy resolution.

The relation between ADC values and the corresponding energies gives the calibration parameters. An example of HPGe spectrum from beam data is shown in figure 3.8: in this spectrum there are the peaks due to both the prompt and the delayed phase; the peaks are narrow, because of HPGe high resolution, and they are well defined over the background.

In the prompt phase the incoming muons have high energy, about 57 MeV/c, they can reach the target walls forming  $\mu\text{Ni}$ ,  $\mu\text{Au}$ ,  $\mu\text{Al}$  and interact with the gas forming  $\mu\text{p}$  and  $\mu\text{O}$ ; however in the prompt phase the only distinguishable

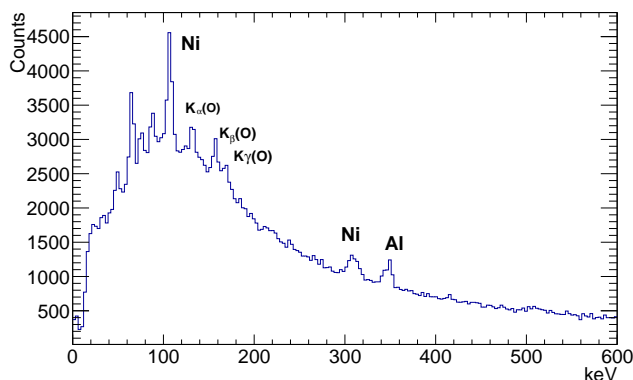


Figure 3.8: Example of HPGe energy spectrum. Both the prompt and delayed emissions are present.

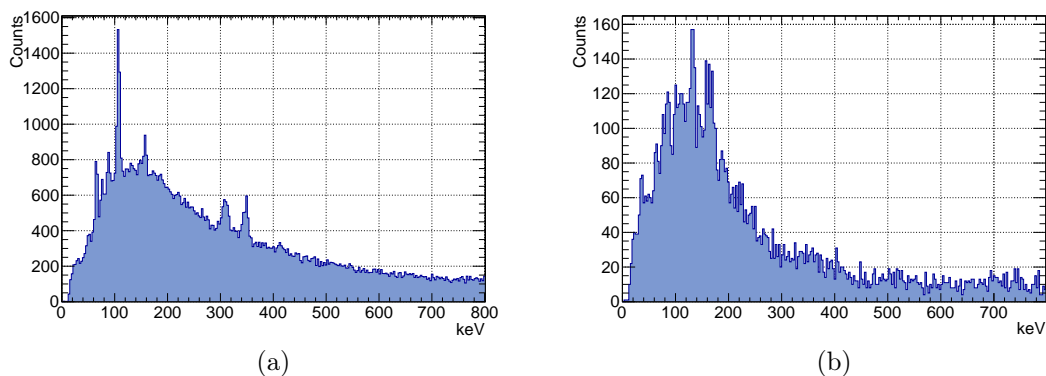


Figure 3.9: (a) Energy spectrum for the prompt phase after the arrival of the first muon pulse; (b) energy spectrum of the delayed phase in (2500, 2600) ns.

lines are due to the target wall de-excitation X-rays because the  $\mu p$  de-excitation energy is too small to be detected and the  $\mu O$  is a small contamination respect to the hydrogen.

In the delayed phase, in which the muons are transferred from  $\mu p$ , the muons have lower energy and only those that are very close to the target walls interact with them; in this phase the situation is reversed and the only visible peaks are due to the  $\mu O$  de-excitation.

In figure 3.9 an example of prompt and delayed energy spectra is shown: in (a) the nickel (102 keV, 310 keV), gold (170 keV) and aluminium (346 keV) peaks are visible, in (b) there are  $K_{\alpha}$  (133.5 keV),  $K_{\beta}$  (158.4 keV) and  $K_{\gamma}$  (167.1 keV) oxygen peaks.

### 3.3.3 Hodoscope

The hodoscope is an useful instrument to monitor the shape, the timing and the position of the muon beam [42].

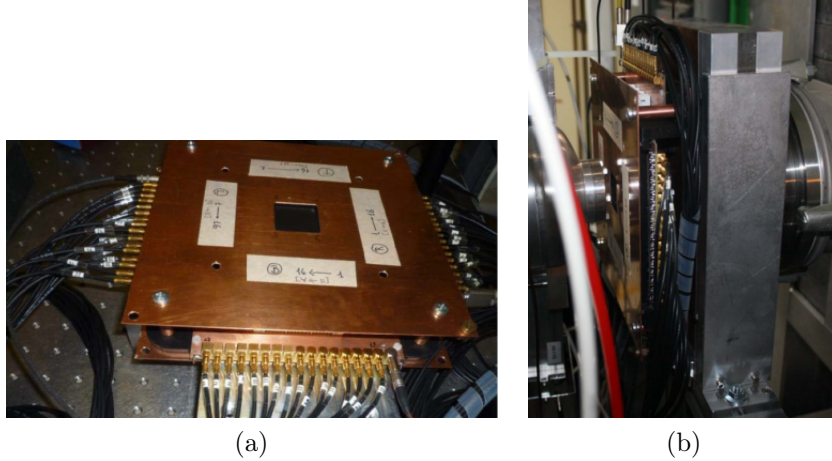


Figure 3.10: (a) Frontal picture of the hodoscope; the LEMO connectors are visible. (b) Hodoscope in place at the experiment: it is placed between the collimator and the gas target.

The central active part is made up of  $32 \times 32$  square shaped Bicron BCF12 scintillating fibers, along x and y direction with 1 mm pitch; the total area is about  $9 \text{ cm}^2$ . Each fiber is read with a Silicon PhotoMultipliers (SiPMs) Advansid ASD-SiPM35 [43]. Pictures of this hodoscope are shown in figure 3.10: one the left the hodoscope in the laboratory, right its positioning on the experiment.

SiPMs are solid state photomultipliers that are single-photon sensitive devices. They are built by a chain of avalanche photodiode on a silicon substrate operating in Geiger mode.

When the muon beam crosses the hodoscope it releases a fraction of its energy on the scintillating fibers that emit light. This light is read by SiPMs and converted into a measurable analog signal. Knowing which fiber produces the signal, the position of the particle that crosses the grid can be measured. The scintillating fibers emitted light is proportional to the particle energy released, hence, with appropriate calibration factors, the number of minimum ionising particles crossing the detectors can be measured.

In FAMU the hodoscope is used to monitor the beam shape and position. In figure 3.11, the beam profile can be seen as function of the x-y position; in this case the hodoscope was not aligned to the beam. The projection on the x and y planes (top right and bottom left panels) are used to better determine the geometry of the beam. One y fiber was not connected to the readout.

Eventually also the total charge distribution for each trigger can be analysed: an example is displayed in figure 3.11 on the top left panel. The charge distribution (in ADC channels) is useful during the beam commissioning. The deposited charge on the hodoscope, proportional to the number of crossing muons, is maximised by varying the beam settings.

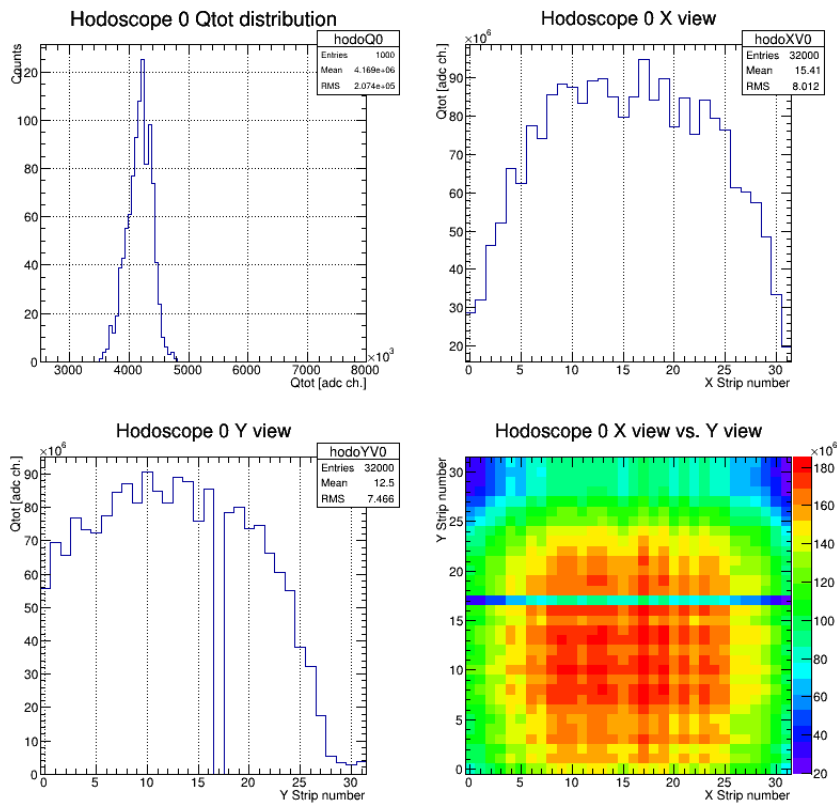


Figure 3.11: Top left: charge distribution. Top right: charge integral as function of the y strip number. Bottom left: charge integral as function of the x strip number. Bottom right: charge distribution as function of x-y position.

## 3.4 Data acquisition and control

The data acquisition system and control is based on detector signals acquisition and a subsequent signals digitalisation and storage.

The  $32 \times 32$  hodoscope channels are read by a one 1 GHz CAEN V1742; the PMT output of the eight LaBr3(Ce) is acquired with 500 MS/s CAEN V1730. For the HPGe different outputs are recorded for a total of seven channels, all of them read by 100 MS/s CAEN V1724.

The experiment trigger is given by the synchrotron machine few hundreds of ns before the arrival of the muon beam double pulse. For each trigger the DAQ saves data in a constant time length of 20  $\mu$ s.

During the acquisition, data are stored locally on disk and processed with a quick look software for monitoring. The data are transferred to CNAF facility where they are processed by an object oriented software written in C++. This software studies each detector wave form extracting the information useful for a complete data analysis. The software is organised in *classes* and each of them controls a different type of detector. In particular, I studied and improved the class that analyses the HPGe data.

## 3.5 HPGe wave form analysis

The wave form is acquired for each detector and with the FAMU software it is possible to perform an offline analysis studying the signal shape or its derivatives. For LaBr3(Ce) scintillators the software performs a fit of the wave function; if there are pile up signals, the software performs a multiple fit and from it, the energy and time parameters are extracted.

For the HPGe the software calculates the signal first derivative and saves the time value of the maximum that is the time at which the derivative passes the zero. To avoid the reconstruction of noise fluctuations as good signals, the software starts analysing the wave form derivative only when it passes the threshold value. I modified the threshold to discard noise events and to identify low energy signals; moreover I added a new variable that is the time at which the signal passes the threshold  $t_{th}$ . The software also saves the energy corresponding to the maximum.

For the saturated signals the software saves both the start and stop time of the saturation.

The data structure is composed of two blocks. The first block contains general information for each trigger, as the absolute time in terms of Linux time (that is the time passed after the first of January 1970), the trigger number, the system temperature; the second block contains specific information about each detected X-ray (event) as the energy, the detector, the pulse high and pulse integral, information on saturated signals.

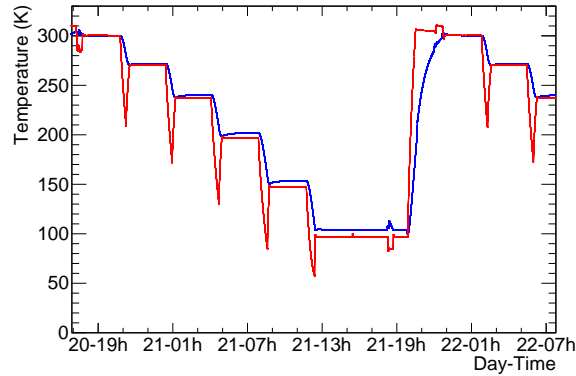


Figure 3.12: Example of temperature variation of the cold head (blue) and of the target (red) from 2016 data. The variations at 21-19h and 21-23h are due to cleaning and refilling of the target.

### 3.6 Temperature control

The target temperature can be adjusted and monitored from remote using a Lakeshore 336 Temperature controller [44]. In particular the target temperature is set by a cold head placed on the upper part of the target.

The temperature control system is made up of the cold head, the compressor and high pressure lines [45]; they form a close circuit in which helium flows as cooling medium. The cold head is where the refrigeration cycle takes place; the compressor, water cooled, provides the necessary helium gas flow rate at the high and low pressure for the cold head. One of the gas lines supplies high pressure helium gas to the cold head, the other gas line returns low pressure helium gas from the cold head. The refrigeration cycle starts with the rotation of the valve disk that opens the high pressure path. The high pressure helium flows in the cold head where, by means of mechanical movements of the valves, it expands and cools. The rotation of the valve disk then opens the low pressure path, allowing the cold gas to flow through the regenerating material which removes heat from the system. Finally, the pressure differential returns the displacer to its original position, and the cycle is completed.

There are four temperature sensors, two on the upper part (A-B) of the cold head and two on the target (C-D). During an acquisition run, the temperature is varied in steps. In order to better understand the thermal cycle it is useful to look at the plot in figure 3.12: the blue line represents the cold head temperature (C-D) whereas the red line represents the target one (A-B). The cold head reaches the temperature faster than the target, so it is fixed at a value below the nominal one and then it is increased again. In this time the target slowly reaches a temperature that is approximately the nominal.

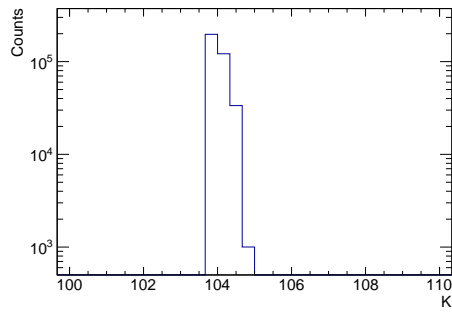
The acquisition starts when the temperature changes less than 1% in 15 minutes.

One acquisition run is about three hours long at a fixed temperature. Between

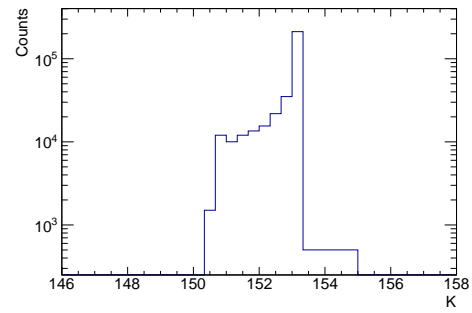
two acquisitions there is a transition phase during which the system reaches the next temperature. For the 2016 data six nominal acquisition temperatures (300 K, 270 K, 240 K, 200 K, 150 K, 100 K) and five intermediate ones (285 K, 255 K, 220 K, 175 K, 115 K) were acquired. For the acquisition phase I considered the real temperature that the system reaches. This is calculated as the mean value between the starting temperature and the final one.

In figure 3.13 the normalised temperature distributions during the acquisition runs are shown: the distributions are peaked at the acquisition temperature. Even if the acquisition is started the temperature could change to reach the nominal value. This is the reason why the distribution is not peaked at one definite value.

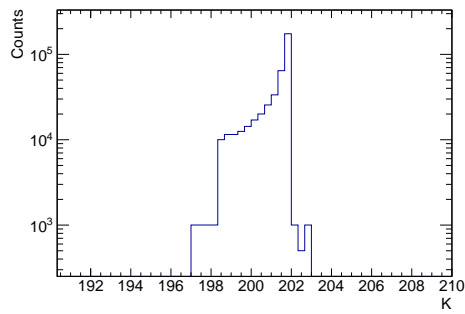
The energy value can be extracted from the temperature distributions. Considering a time interval, for each temperature the corresponding Boltzmann energy distribution can be found; the convolution of all the Boltzmann distribution is peaked at the mean energy of the system.



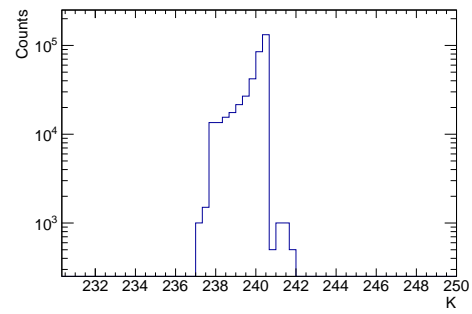
(a) Nominal T = 100 K



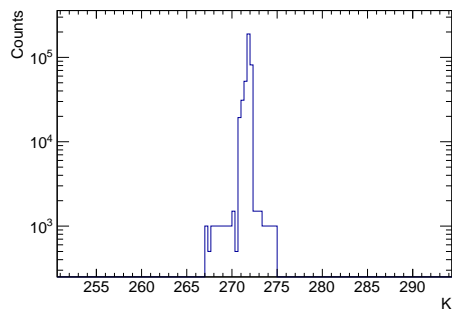
(b) Nominal T = 150 K



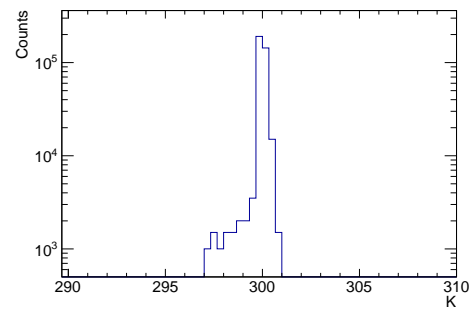
(c) Nominal T = 200 K



(d) Nominal T = 240 K



(e) Nominal T = 270 K



(f) Nominal T = 300 K

Figure 3.13: Temperature distributions during acquisition run.

# Chapter 4

## Data analysis

In the FAMU experiment there are four HPGe detectors, previously described in chapter 3. For each detector a different number and typology of wave functions were acquired:

- ORTEC GEM-S (Mi): output from the pre-amplifier, from the amplifier, and the one from the fast amplifier;
- ORTEC GLP (Mi): output from the pre-amplifier and from the amplifier;
- ORTEC GEM-S (RIKEN) and ORTEC GMX (RIKEN): output from the amplifier.

Pre-amplified signals have short rise time ( $\approx 100$  ns) and a very long decay tail ( $\approx$  tens of  $\mu$ s), as it can be seen in figure 3.6.

In a high rate experiment, as FAMU, the probability of having pile up increases. If two or more pre-amplified signals pile up, because of the long tail, they can reach an amplitude that is higher than the system upper limit, so the acquisition system saturates.

When the acquisition system is saturated, it remains blind for a variable period of time, that in this context we call dead time. To avoid this problem, the pre-amplified signal is sent to an amplifier, which amplifies and shapes the waveform giving, as output, a semi-gaussian signal. The shaping time of the amplified signals coming from ORTEC GEM-S (Mi) and from ORTEC GLP is  $2 \mu$ s.

Using shaped wave form, the pile up signals problem is reduced because the decay tail goes down faster than the pre-amplified one. However, if two signals are very close in time, they are integrated together giving an output signal with amplitude proportional to the sum of the two.

Also the output from the fast amplifier is recorded; this wave form is semi-gaussian with 200 ns shaping time. This gaussian is narrower (FWHM  $1 \mu$ s) respect to the amplified one (FWHM  $4 \mu$ s) permitting the identification of a greater number of signals.

Even though signals are shaped, in a high rate environment, saturation can occur at different levels in the acquisition chain: from the crystal to the electronic. In FAMU, the saturation is due to the acquisition system. Infact, signals are recorded by means of a 14-bit digitizer: it is suitable to reconstruct low energy signals of hundred of keV, that are the energies of the interesting transition, but it has not enough channels for higher energy (order of MeV) signals reconstruction. Therefore, the two main problems that determine the correct event (X-ray) reconstruction are the dead time and the saturation.

The two corrections I applied on data are due to the saturation of the detector, that causes a dead time of the acquisition, and to the loss of efficiency due to an incorrect reconstruction of the number of events and energy. Both corrections have an effect on the number of events in a time interval; so they are fundamental for the transfer rate determination, as discussed in chapter 2.

In the following analysis I used only the data acquired with the fast amplifier of the ORTEC GEM-S (Mi) detector; it has a short decay tail compared to the amplified one, so the number of pile up signals is reduced. Shaped signals are integrated for a longer time ( $2 \mu\text{s}$ ) respect to the fast (200 ns) ones, so the fast signals are better for the time analysis.

Pre-amplified signals, instead, require a shape analysis that is currently under study.

## 4.1 Dead time correction

When a saturation event occurs, the acquisition system is blind for a time that depends on the signal amplitude. In particular, as shown in figure 4.1, the signal grows up to the digitizer saturation; then the ADC remains blind until the signal amplitude decreases under the saturation threshold. The time interval corresponding to the saturation is determined by the plateau length, that depends on the signal amplitude and is indicated in the figure by the two red lines. This effect is more important in the prompt phase than in delayed one since there are more events. To correct data for saturation I realised a dead time correction curve. By definition all triggers have a length of  $20 \mu\text{s}$ .

I measured the number of events for which the signal saturated as function of time in the  $20 \mu\text{s}$  time window. I normalised this number to the first time bin, which contains only low noise energy events prior to the arrival of the beam. For this distribution, the time correction curve shown in figure 4.2 is obtained.

In the time interval [4000, 5000] ns there is a loss of about 20% of events.

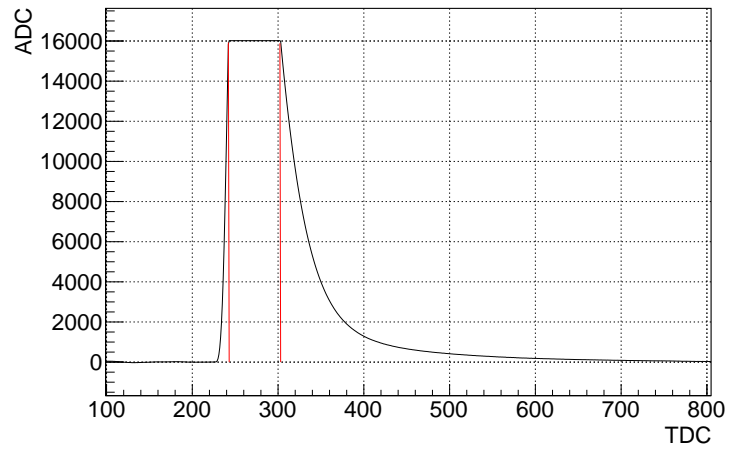


Figure 4.1: Example of a fast saturated signal; the red lines indicate the initial and final saturation time.

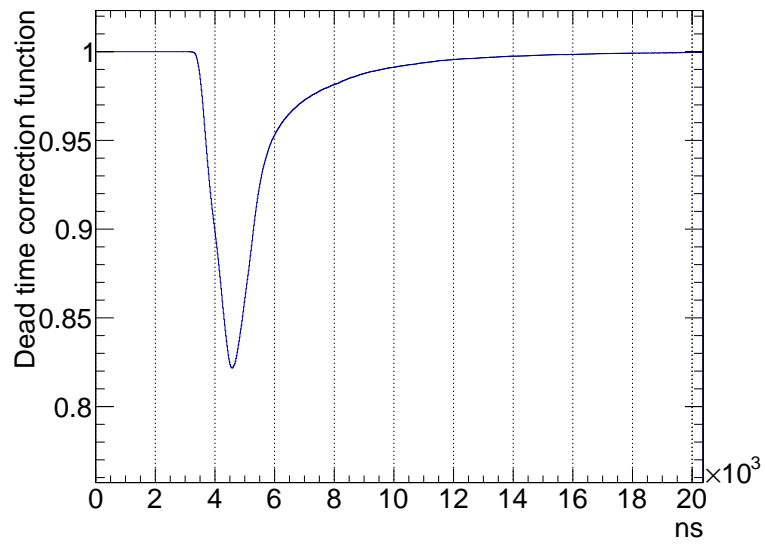


Figure 4.2: Dead time correction curve for the fast amplified signal at 300 K.

## 4.2 Pile up rejection selection

If pile up events are identified and correctly reconstructed they are treated as good events and used in the data analysis. When these events are not identified, they cause a wrong event energy reconstruction: their identification, even if complicated, it is necessary.

In order to reject pile up events incorrectly reconstructed I studied the rise time behaviour. In this analysis, I defined the quantity  $\Delta RT = t_{max} - t_{th}$  as the "rise time" where  $t_{th}$  is the time at which the signal derivative passes the software threshold (values are specified in chapter 3) and  $t_{max}$  is the time of the signal maximum.

First of all, I analysed the calibration data, because their rate is lower than the acquisition rate, and the number of pile up signals is reduced.

### 4.2.1 Rise time of calibration data

Calibration data were acquired with a Co source and with a mixed source of Cs, Am, Sr. I studied the distribution of  $\Delta RT$  considering the events that have an energy around the Co peak [120, 140] keV or around the Cs peak [650, 670] keV. I chose these two energy regions for two reasons: to understand what happens in the interval [120, 140] keV that is the same in which the  $K_\alpha$  oxygen peak lays and to analyse how the  $\Delta RT$  behaviour changes at higher energies.

In figure 4.3, blue line, the  $\Delta RT$  distribution for calibration data is shown, after the selection of [120, 140] keV interval. This distribution is centered around 330 ns, with a fast rise but with a right tail.

Even if the nominal rise time is of about 200 ns, the rise time distribution is peaked at 330 ns because of the time required by the electronic chain and by the signal formation.

In order to understand the reason why the distribution has this particular shape instead of been peaked at one defined value, I analysed the wave form of signals which have a  $\Delta RT$  of 310 ns or of 350 ns. The width of the distribution is related to the software event reconstruction: there is an uncertainty due to the  $t_{max}$  identification, that is where the signal derivative passes the X-axis, and in the  $t_{th}$  determination, based on when the derivative passes the threshold (see section 3). Noise fluctuations can change the rise time of the signal. This uncertainty is reflected in the spread of the  $\Delta RT$  distribution. An example of this phenomenon is shown in figure 4.4: in the top panel the signal waveform is shown. Baseline fluctuations are visible up to 500 TDC, where the signal arises. If the noise is large the signal is shifted, and these fluctuations have an effect on the  $t_{max}$  determination. On the bottom the derivative of the signal is represented: also in this case there are baseline fluctuations which increase the uncertainty in the  $t_{th}$  determination.

The second aspect to be investigated is the presence of a right tail. Analysing the output of the fast amplifier for these events, I noticed that the fast amplified

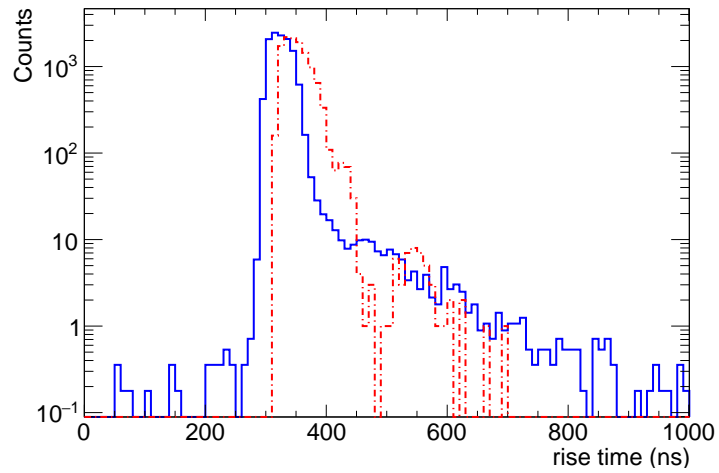


Figure 4.3: In blue  $\Delta RT$  distribution of Co, in red the Cs one. The peaks of the two distributions are shifted of about 30 ns.

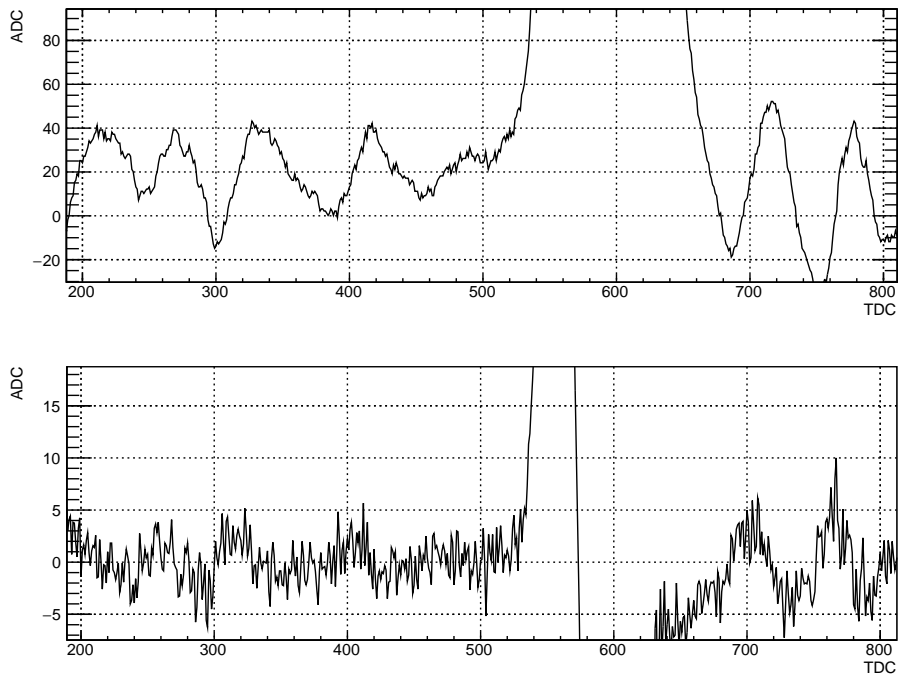


Figure 4.4: Top panel: fast amplified wave form, zoomed in the first region: there are a lot of noise fluctuations. Bottom panel: derivative of the wave form.

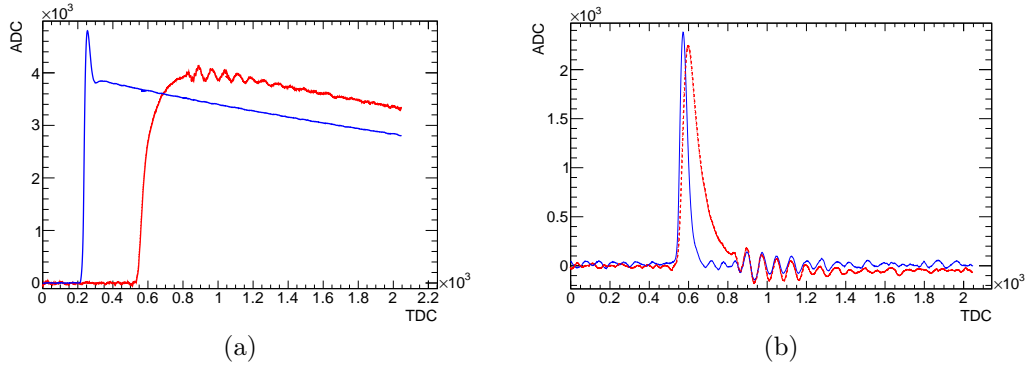


Figure 4.5: (a) In blue an example of a "typical" pre-amplified signal; in red an example of pre amplified signal with  $\Delta RT > 400$  ns. (b) Comparison between fast amplified wave: in blue the one associated to the blue pre-amplified in figure (a) ( $\Delta RT \approx 320$  ns), in red the signal associated to the red one ( $\Delta RT > 400$  ns).

signal is different from the previous ones. In figure 4.5(b) a comparison between two fast amplified signals with  $\Delta RT \approx 320$  ns (blue) and  $\Delta RT > 400$  ns (red) is shown. If  $\Delta RT > 400$  ns the fast amplified signal shares a right tail that decays exponentially. I chose  $\Delta RT > 400$  ns because it permits to discard the right tail by keeping 98% of the events. In figure 4.5(a) the comparison between the corresponding pre-amplified wave forms is shown. The pre-amplified signal represented with the red line respects the condition  $\Delta RT > 400$  ns (on the corresponding fast amplified): the difference is the wave form shape. The reason for this strange signal shape is unclear. The red kind of signals are not observed in the laboratory where the detector is tested in a controlled situation; therefore these signals could be due to acoustic noise induced on the detector by the cold head or to the way the energy was released in the active volume of the detector.

In figure 4.5 for both the pre and, as a consequence, the fast amplified signals there are noise fluctuations on the red signal right tail: these oscillations are due to acoustic noise and, even though they are wide, they do not pass the analysis software threshold.

The energy spectrum in the [120, 140] keV energy interval of the events that respect the  $\Delta RT > 400$  ns condition is shown in figure 4.6. Since in this energy interval there are two Co lines (at 122 keV and 136 keV) that are not visible in this spectrum, the events belonging to the  $\Delta RT > 400$  ns selections are part of the background.

The  $\Delta RT$  distribution for data in the energy region around the Cs peak [650, 670] keV is shown in red in figure 4.3. In this case, the distribution is peaked around 350 ns, and it has a right tail with less counts than the Co one. The distribution is spread in the [310, 380] ns interval because of derivative fluctuations, as the Co case. Also in this case I analysed the wave form of the events in the right tail: they do not share a particular shape as in figure 4.5(a) (blue line). The energy spectrum of these events ( $\Delta RT > 400$  ns), that is represented in figure 4.7, decreases exponentially. Since the source used for the calibration contains various

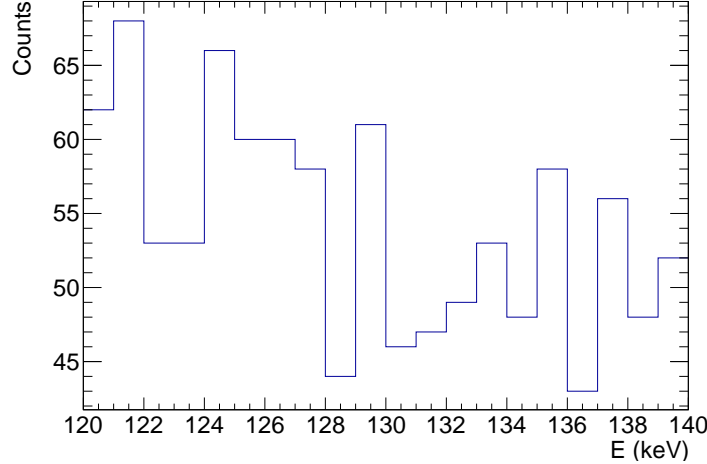


Figure 4.6: Energy distribution in [120, 140] keV of events with  $\Delta RT > 400$  ns.

radioactive elements, I supposed that the events in [650, 656] keV energy range could be pile up of X-rays coming from different elements. Analysing the pre-amplifier wave form shape for the events in the same energy range it was noticed the presence of pile up. In particular, the sum of 136 keV of Co to 511 keV of electron-positron annihilation gives 647 keV. To prove this hypothesis, I realised the events energy spectrum selecting data with energy in the range [550, 670] keV and with  $\Delta RT > 400$  ns. The result is shown in figure 4.8: the energy spectrum is peaked at 647 keV, dashed red line, so the right tail is mainly formed by pile up events.

In the [656, 670] keV region the energy spectrum is flat, even if Cs shows a line at 662 keV. The conclusion, as for Co, is that the events with  $\Delta RT > 400$  ns that belong to the [656, 670] keV region, are background events.

The comparison between the two  $\Delta RT$  distributions at 136 and 662 keV is displayed in figure 4.3. The two distributions are shifted by 30 ns. The rise time, infact, has a small dependence on the signal amplitude.

The events with  $\Delta RT > 400$  ns are characterised by pile up or by wave forms that are wrongly reconstructed by the software; this cut identifies a category of bad events that has to be discarded.

## 4.2.2 Rise time of beam data

I considered then the data set acquired with the  $H_2 + 0.3\%O_2$  gas mixture. I studied the  $\Delta RT$  distribution for the beam data in an energy range of [120, 400] keV; in this case a right and also a left tail appear, as it is visible in figure 4.9. To understand the nature of these tails I analysed the events with  $\Delta RT < 280$  ns and  $\Delta RT > 400$  ns separately, and for each case I studied energy,  $t_{th}$  distribution, that is the time at which the signal derivative passes the software threshold, and wave form shape.

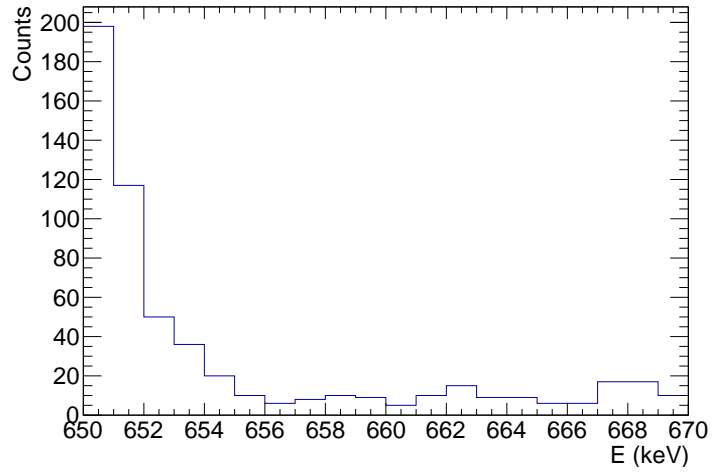


Figure 4.7: Energy distribution in [650, 670] keV of events with  $\Delta RT > 400$  ns.

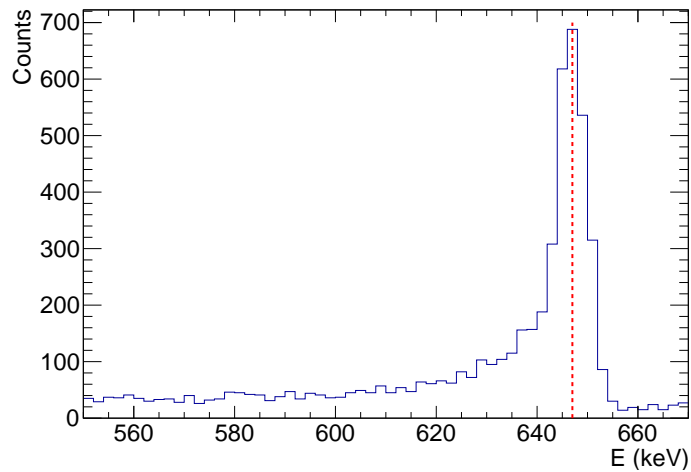


Figure 4.8: Energy distribution of events with  $\Delta RT > 400$  ns in [550, 670] keV interval. The red line indicates the 647 keV energy.

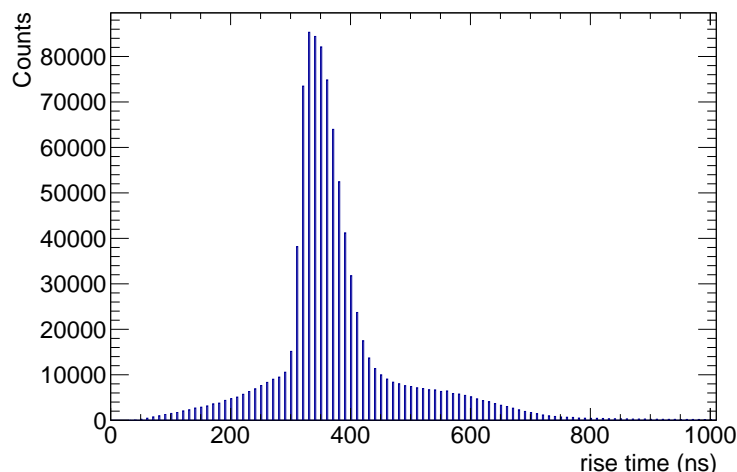


Figure 4.9:  $\Delta RT$  distribution for acquired data.

The energy spectrum for  $\Delta RT < 280$  ns is shown in figure 4.10. The only visible peak is in the [130, 140] keV region and the behaviour decreases exponentially, so it seems that the majority of this kind of events appears in the delayed phase. To prove this hypothesis, it is useful to analyse the  $t_{th}$  distribution, presented in figure 4.11, for the fast signals. The  $t_{th}$  spectrum starts at about 2000 ns, that is when the second pulse arrives, that is evident from the comparison to time spectrum in figure 4.12. I can conclude that the majority of events with  $\Delta RT < 280$  ns occurs in the delayed phase.

The pre-amplifier wave form is characterised by pile up events, that are very close in time, as can be seen in figure 4.13. The corresponding fast analysis distinguishes the two signals but associates the wrong  $t_{th}$  to the second signal. An example is shown in figure 4.14: the two fast wave forms are detectable and the signal derivative identifies two peaks assigning to  $t_{th}$  the time value at which the signal derivative passes the threshold. In this case, however,  $t_{th}$  of the second signal is not the time at which the signal arrives, that could be evaluated properly fitting the fast wave function and extrapolating the intersection point between the wave form fit and the x-axis. The time difference in the  $t_{th}$  calculation using the two explained methods is responsible of the  $\Delta RT$  distribution left tail. Even if the two signals are in pile up and their  $t_{th}$  can be slightly shifted, their energy is correctly reconstructed, therefore these events are not discarded.

I repeated the same analysis also for the case  $\Delta RT > 400$  ns; both energy and time spectrum are different from the previous case. The energy spectrum in figure 4.15 shows the aluminium and nickel peaks and it seems to indicate that these events can appear also in the prompt phase. By analysing the  $t_{th}$  spectrum, shown in figure 4.16, and comparing it with the overall spectrum, it can be observed that  $\Delta RT > 400$  ns events are distributed in all the time window.

The wave form analysis shows two pre-amplified piled up signals but only one fast.

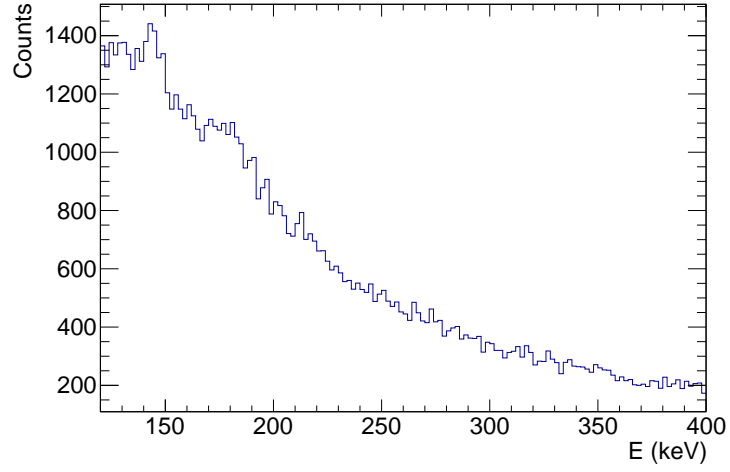


Figure 4.10: Energy distribution for data with  $\Delta RT < 280$  ns.

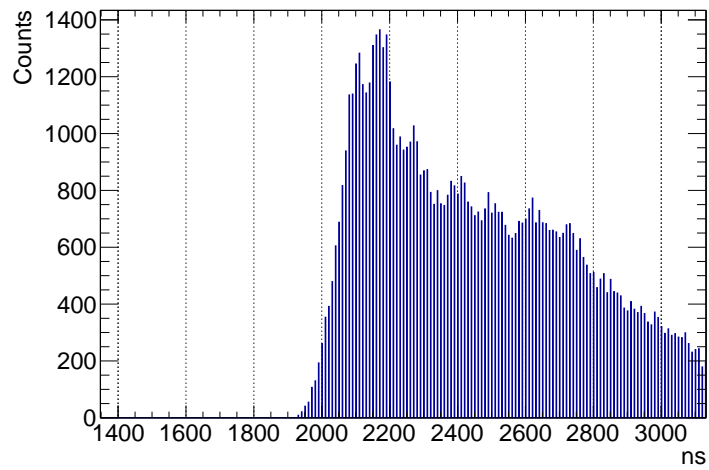


Figure 4.11:  $t_{th}$  distribution for events with  $\Delta RT < 280$  ns.

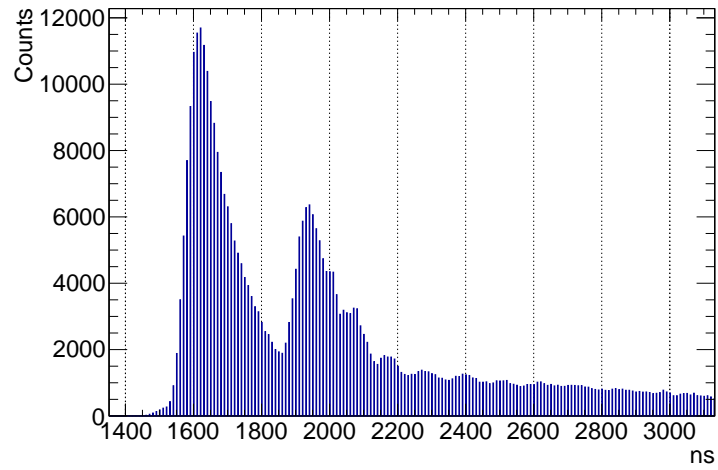


Figure 4.12: Time spectrum for all the events at  $T=300$  K.

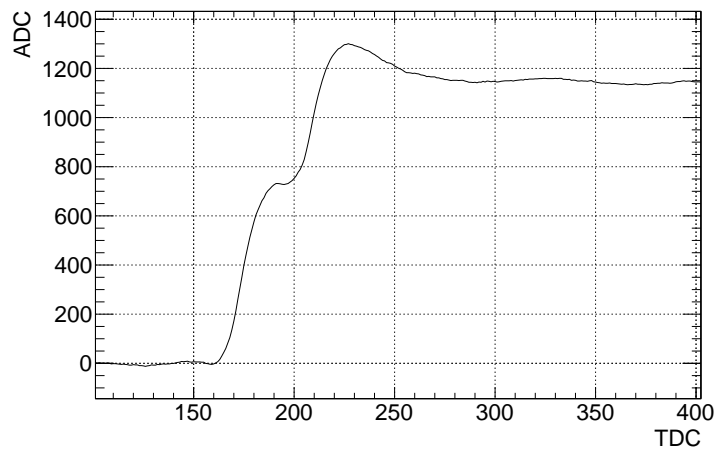


Figure 4.13: Example of two pre amplified signals  $\Delta RT < 280$  ns.

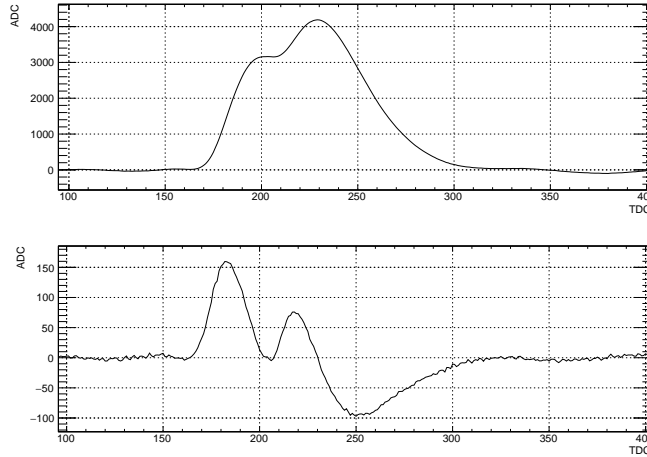


Figure 4.14: Example of two fast reconstructed signal with  $\Delta RT < 280$  ns. Top panel: fast amplified wave form. Bottom panel: corresponding derivative wave form.

As shown in figure 4.17(a), part of the events that satisfy  $\Delta RT > 400$  ns condition is characterised by two piled up pre-amplified signals that are so closed to be reconstructed as one by the software. The corresponding fast amplified output, showed in figure 4.17(b), is reconstructed as only one signal by the analysis software because the variation in the rise tail is too small to be identified.

The conclusions of this analysis on beam data are that the rise time  $\Delta RT$  depends on the event energy and that events with  $\Delta RT > 400$  ns correspond to pile up signals.

A new data selection,  $\Delta RT < 400$  ns, can be used; this cut is justified by the fact that  $\Delta RT > 400$  ns events are piled up events that must be rejected. In this way I can reduce background and discard wrong reconstructed energies. However, a part of pile up events still remains in the sample, since it is reasonable that two X-rays arriving in coincidence in the detector generate a signal with  $\Delta RT < 400$  ns. Further analysis on pile up events reconstruction and identification will be done, also by means of the simulation.

In the following analysis,  $\Delta RT > 400$  ns cut is applied to obtain a sample with a reduced number of pile up events. As a consequence, an efficiency correction as function of time and as function of energy must be estimated, to take into account the time and energy dependence of the selection.

### 4.3 Pile up rejection cut efficiency

I obtained the efficiency curve as a function of time from beam data in two different ways: considering  $t_{th}$  and considering the  $\Delta RT$ .

In the first method I defined a large number of bins (200), with fixed dimension (100 ns). Then I measured the percentage of events that pass the selection  $\Delta RT < 400$  ns for all bins and energies as function of time  $t_{th}$ . The curve I obtained is shown in figure 4.18. In the worst case there is a loss of 40% of events. This curve

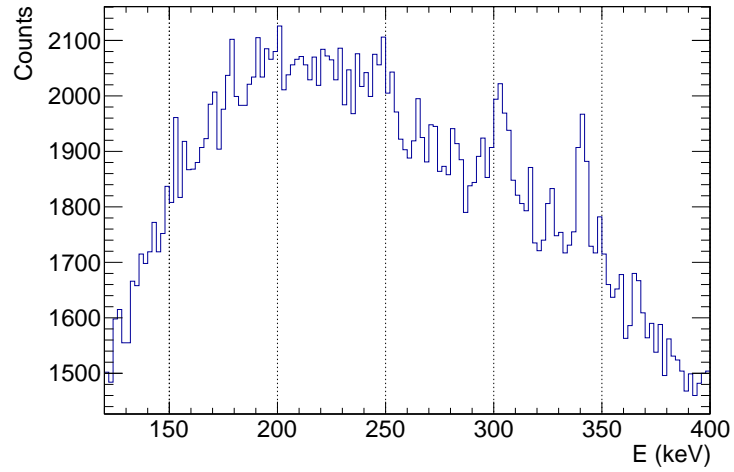


Figure 4.15: Energy distribution for data with  $\Delta RT > 400$  ns.

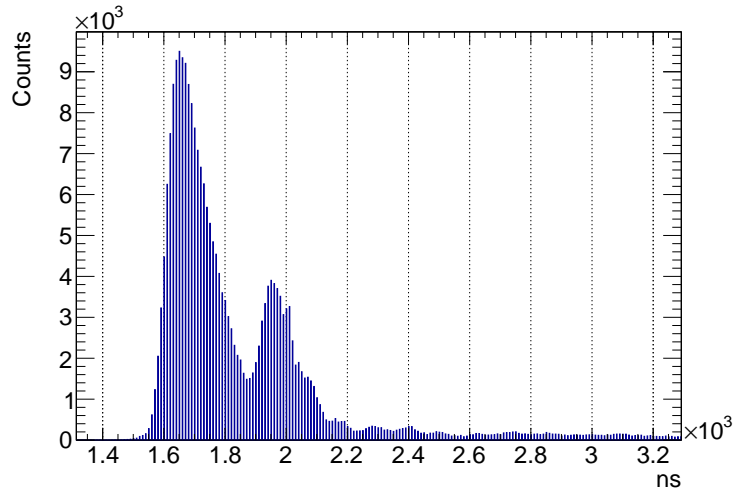


Figure 4.16:  $t_{th}$  distribution for events with  $\Delta RT > 400$  ns.

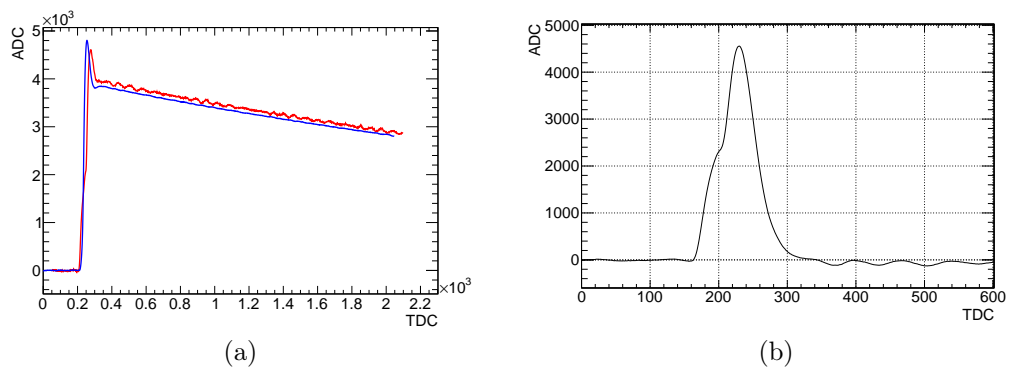


Figure 4.17: (a) In blue a typical pre-amplified signal compared to one that is the result of two close pile up signals, in red. (b) Example of fast amplified wave form for data with  $\Delta RT > 400$  ns: there are two signals but the software reconstructs only one.

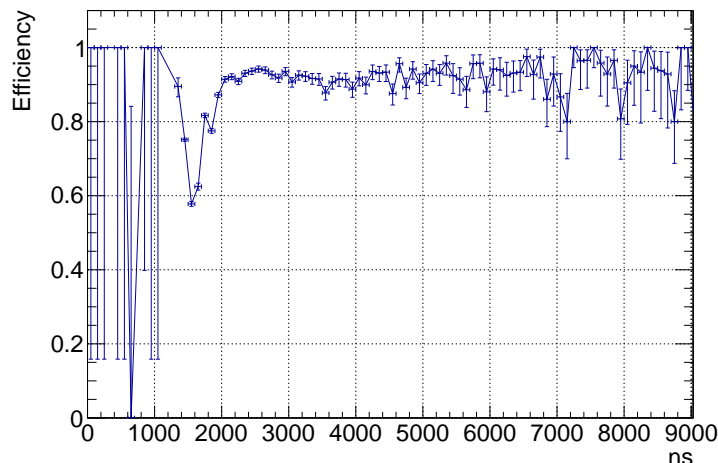


Figure 4.18: Efficiency correction curve - first method (using  $t_{th}$ ).

is constructed assigning the event to the time  $t_{th}$ , which is anticipated respect to the moment when the pile up occurs.

The second method is based on a procedure analogous to the dead time correction.

I integrated the time interval  $]t_{th}, t_{max}[$  when  $\Delta RT > 400$  ns over all the events; I normalised this number to the first time bin, which contains events prior to the arrival of the beam, in which there are no pile up events. I obtained the time correction curve presented in figure 4.19. As it can be seen, the correction involves a loss of about 80% of events between 1800 ns and 2200 ns, that is when the second pulse arrives.

The first way under estimates the correction, since pile up occurs during a time interval; the second approach is an over estimation because it attributes an entire time interval to the pile up event. Moreover, the point of the minimum is shifted due to the different timing of the two methods. The second method was chosen for the data analysis. The difference between the two methods is taken into account in the evaluation of the systematic error described in section 4.6. Notice, however, that this correction is relevant in 1500-2500 ns, corresponding to the prompt phase.

$\Delta RT$  spectra evaluated in different energy ranges are shifted, as already discussed in section 4.2. In particular, the higher is the energy, the more the spectra are shifted to the right. So, maintaining the  $\Delta RT$  selection cut fixed, I reject more events at higher energy. It is reasonable to obtain an efficiency curve with decreasing behaviour at higher energies because the correction has to compensate the higher number of rejected events.

Since the energy spectrum changes with time, and since there is a  $\Delta RT$  dependence on time, it is natural conclude that there is also an energy dependence on  $\Delta RT$ . In order to understand if it is a great correction and in which time and energy region it is important, I realised three energy correction curves, for three

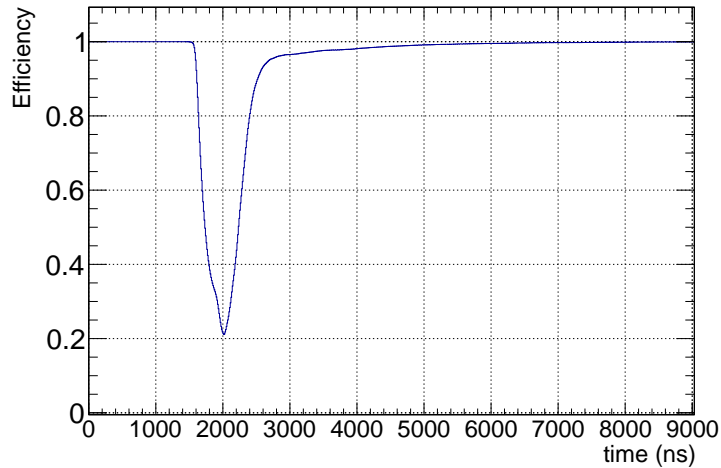


Figure 4.19: Efficiency correction curve - second method (using  $\Delta RT$ ).

time intervals, before, after and during the first  $\mu$  pulse.

First, I chose a time interval and I considered the energy spectrum in that time region; I did the same but only with the events with  $\Delta RT < 400$  ns; the percentage of events that pass the selection as function of energy is shown in figure 4.20.

In figure 4.20(a), 4.20(b) and 4.20(c) there are the curves corresponding respectively to the time intervals [1600, 1900] ns, [1900, 2200] ns and [2200, 2500] ns.

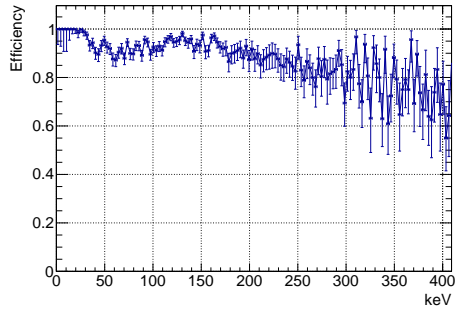
Notice that this efficiency estimation is biased, since it includes also events that have a wrong energy reconstruction. A better estimation can be obtained using the simulation, an on going work. This study on real data is useful since it gives the indication that there is a negligible energy dependence of the  $\Delta RT$  selection cut in the energy region of interest.

## 4.4 Transfer rate measurement

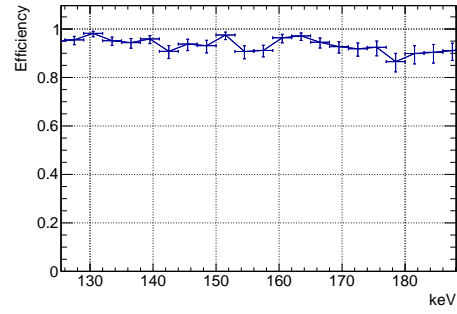
The first steps in the transfer rate measurement analysis are the data selection and the implementation of correction functions. I applied the  $\Delta RT$  selection cut and I chose the [140, 180] keV energy interval, that is around the oxygen peaks. For each energy in that interval I divided the corresponding time distribution by the dead time correction curve and by the rise time selection efficiency. Then I studied the time evolution of the energy distributions.

### 4.4.1 Background subtraction

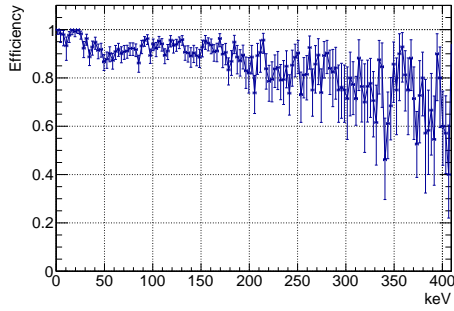
The correct identification of the number of events at oxygen peaks is fundamental for the transfer rate determination; to achieve this goal, a correct background subtraction is necessary.



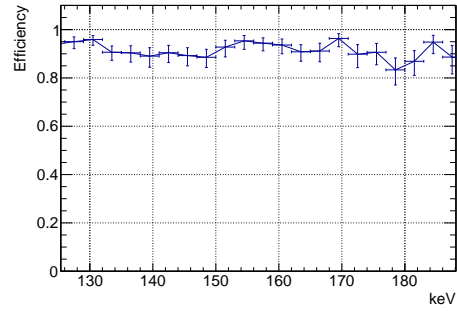
(a) Energy correction if  $t \in (1600, 1900)$ .



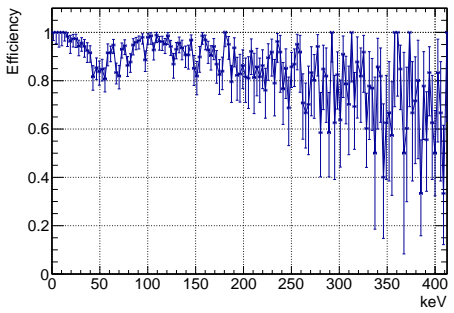
(b) Energy correction if  $t \in (1600, 1900)$ , zoom.



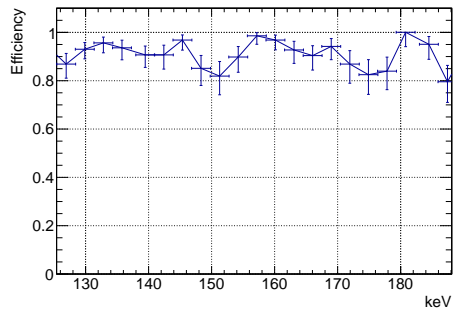
(c) Energy correction if  $t \in (1900, 2200)$ .



(d) Energy correction if  $t \in (1900, 2200)$ , zoom.



(e) Energy correction if  $t \in (2200, 2500)$ .



(f) Energy correction if  $t \in (2200, 2500)$ , zoom.

Figure 4.20: Evolution of energy efficiency curves with time interval, at  $T=300$  K.

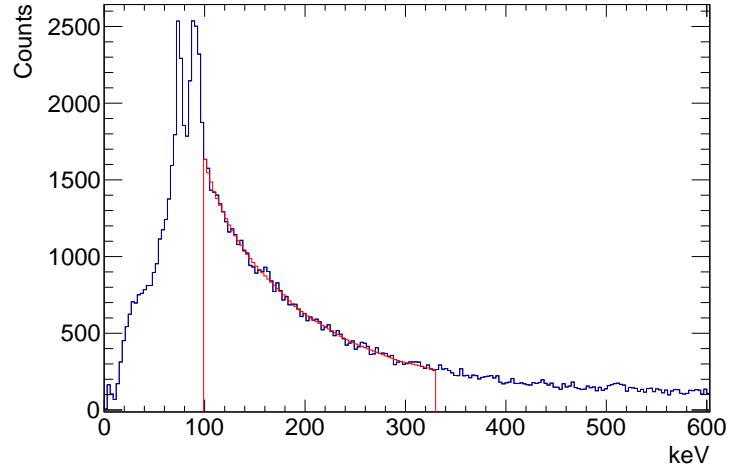


Figure 4.21:  $H_2 + CH_4$  complete spectrum, background estimate in red.

The background estimate can be done in different ways: by using dedicated spectroscopy tools, via pure hydrogen energy spectrum subtraction, by fitting with an exponential function the background spectrum or by making use of data acquired in  $H_2 + CH_4$ .

The best solution is to use data acquired in pure hydrogen because they reproduce the same experimental conditions (same pressure and temperature) but without the oxygen lines. However, since the sample of  $H_2$  acquired in 2016 has not enough statistic, I decided to use data acquired using the  $H_2 + CH_4$  gas mixture.

It is possible to use  $H_2 + CH_4$  for the background estimation because even if there are carbon peaks, these are at lower energies (about 90 keV) respect to the oxygen ones. The background estimation is obtained considering the energy spectrum above 100 keV and normalising the data respect to the oxygen spectrum. Since also the  $H_2 + CH_4$  data are affected by saturation and pile up, before the background evaluation, data were corrected by their dead time and efficiency curves, obtained as for oxygen.

The  $H_2 + CH_4$  complete spectrum is displayed in figure 4.21; the estimate of the  $H_2 + CH_4$  background in [100, 330] keV is obtained with a smoothing procedure, red line.

#### 4.4.2 Peak identification

To find the transfer rate, it is necessary evaluate the number of events at oxygen peak, that is the region in which there is more statistics. Fixed the time interval, I considered the corresponding energy spectrum. At this point the background, previously estimated, was subtracted giving the clean signal. The events considered for the transfer rate calculation stand in an energy interval [140, 180] keV. The choice of the energy lower limit was due to avoid wrong background subtraction.

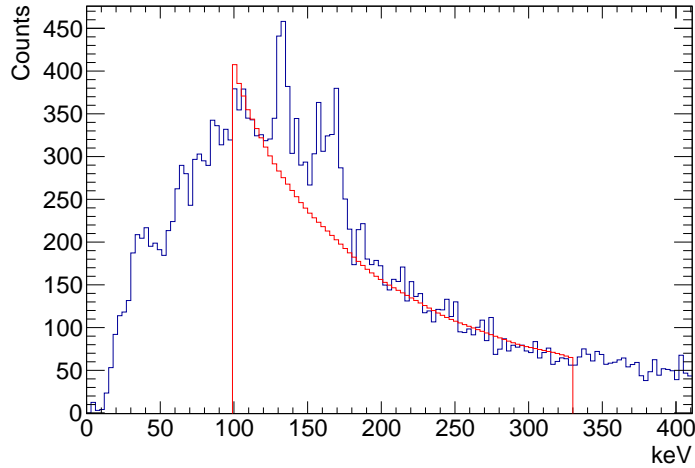


Figure 4.22:  $H_2 + O_2$  energy spectrum with  $H_2 + CH_4$  background (in red). Around 100 keV the background is over estimate.

Since background estimation comes from another spectrum, around 100 keV it could contain a  $H_2 + CH_4$  signal tail as can be seen in figure 4.22 so, around 100 keV, the background is over estimated.

The upper limit selection was made to consider the three oxygen peaks to have more statistics.

The rate number is given by the number of events at the peaks normalised for the width of the time interval. This procedure was repeated for all the time intervals, that have an exponentially increasing amplitude to take into account the decreasing number of events with time.

In this analysis, I chose three time intervals: [2500, 3042] ns, [3042, 3702] ns, [3702, 4506] ns. The first and the last time bin were chosen looking when the oxygen peaks appear and when they disappear in the energy spectra. The signal for each interval is represented in figure 4.23. The values of the rate as function of the central value of the time interval are plotted in figure 4.24; the behaviour is exponentially decreasing as expected.

## 4.5 Fit function

In order to find the proper fit function, I took into account the variation of the number of  $\mu p$  on time. The emitted oxygen X-rays depend on the number of muons and on the transfer rate that is the goal of this measurement.

The variation of number of muonic hydrogen atoms  $N_{\mu p}$  present in the target in the time  $dt$  can be expressed by the following formula:

$$dN_{\mu p}(t) = S(t)dt - N_{\mu p}(t)\lambda_{dis}dt, \quad (4.1)$$

where  $S(t)$  is the number of muonic hydrogen generated in the time interval  $dt$ ,

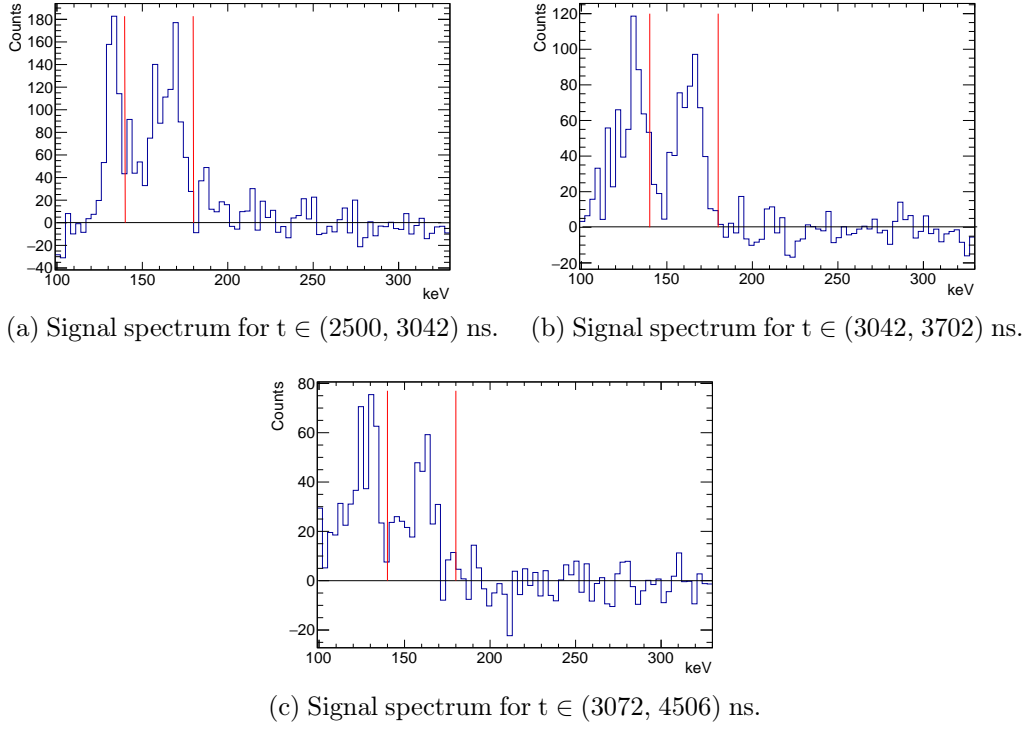


Figure 4.23: Evolution of signal spectrum with time interval in the case  $T=300$  K. The two vertical red lines locate the extremes of the energy interval.

and  $\lambda_{dis}$  is the total disappearance rate of the muonic hydrogen atoms:

$$\lambda_{dis} = \lambda_0 + \phi (c_H \Lambda_{pp\mu} + c_d \Lambda_{pd} + c_{O_2} \Lambda_{pO_2}). \quad (4.2)$$

Here  $\lambda_0$  is the rate of disappearance of the muons bounded to proton (that includes both muon decay and nuclear capture),  $c_H$ ,  $c_d$ ,  $c_{O_2}$  are the concentrations of hydrogen, deuterium, and  $O_2$  in the gas target, related to the number densities of the latter,  $N_H$ ,  $N_d$ , and  $N_{O_2}$ , by:

$$c_H = N_H/N_{tot}, \quad c_d = N_d/N_{tot}$$

$$c_{O_2} = N_{O_2}/N_{tot}$$

$$N_{tot} = N_H + N_d + N_{O_2}$$

$$c_H + c_d + c_{O_2} = 1,$$

$\Lambda_{pp\mu}$  is the formation rate of the  $pp\mu$  molecular ion in collision of  $\mu p$  with a hydrogen nucleus,  $\Lambda_{pd}$  denotes the muon transfer rate from  $\mu p$  to deuterium, and  $\Lambda_{pO_2}$  is the muon transfer rates from  $\mu p$  to the oxygen. The  $pp\mu$  formation and muon transfer rates are all normalised to the liquid hydrogen number density (LHD)  $N_0 = 4.25 \cdot 10^{22} \text{ cm}^{-3}$ , and  $\phi$  is the target gas number density in LHD units. The unknowns in equations 4.1 and 4.2 are  $S(t)$  and  $\Lambda_{pO_2}$ .  $\Lambda_{pO_2}$  is the free parameter that is going to be measured.

### 4.5.1 Parameters determination

$c_{O_2}$  is the atomic concentration of  $O_2$  in  $H_2$  mixture; it is defined as:

$$c_{O_2} = \frac{n_O}{n_O + n_H} \quad (4.3)$$

where  $n_O$  and  $n_H$  are the numbers of oxygen and hydrogen atoms respectively.

The molecular concentration of a gas molecule  $O_2$  in a mixture with  $H_2$  is:

$$C_{O_2} = \frac{N_{O_2}}{N_{O_2} + N_{H_2}} \quad (4.4)$$

with  $N_{O_2}$  the number of oxygen molecules and  $N_{H_2}$  the number of  $H_2$  molecules ( $n_H = 2N_{H_2}$ ). The value of the atomic concentration of oxygen  $c_{O_2}$  can be obtained knowing the mass concentration of the oxygen  $w_{O_2}$  in the mixture:

$$w_{O_2} = \frac{N_{O_2} \cdot M_{O_2}}{N_{O_2}M_{O_2} + N_{H_2}M_{H_2}} = \frac{C_{O_2} \cdot M_{O_2}}{C_{O_2}M_{O_2} + C_{H_2}M_{H_2}} \quad (4.5)$$

Given  $w_{O_2}$  and  $C_{O_2} + C_{H_2} = 1$ , the value of the molecular concentration of  $O_2$  is:

$$C_{O_2} = \frac{w_{O_2}M_{H_2}}{M_{O_2} + w_{O_2}(M_{H_2} + M_{O_2})} \quad (4.6)$$

From the molecular concentration, it is easy obtain the atomic concentration  $c_{O_2}$ .

The  $c_d$  value is the natural deuterium concentration in the mixture; the deuterium concentration respect to the number of atoms of hydrogen was measured and it was equal to  $c_{d(H)} = 1.359 \cdot 10^{-4}$  [46]. To find the value of  $c_d$  I have to normalise  $c_{d(H)}$  respect to the total number of atoms and then respect the molecular concentration. The general formula for a mixture with a molecule  $X$  with a total number  $a$  of atoms is:

$$c_{d(H_2+X)} = \frac{n_d}{n_X + n_H} = \frac{2c_{d(H)}(1 - C_X)}{2 + (a - 2)C_X} \quad (4.7)$$

$c_H$  is the atomic concentration of hydrogen. Its value is  $c_H = 1 - c_{O_2} - c_d$ .

In this case, the target is filled with  $H_2 + O_2$  gas and  $w_{O_2} = 0.3\%$ ; the values are:

- $c_{O_2} = 1895.2 \cdot 10^{-4}$ ;
- $c_d = 1358.74 \cdot 10^{-4}$ .

$\phi$  is the target density in LHD units. The experiment is performed at constant  $\phi$ , at fixed volume but with varying pressure and temperature.

The number of particles per unit of volume is

$$\frac{N}{V} = \frac{p}{RT} N_a, \quad (4.8)$$

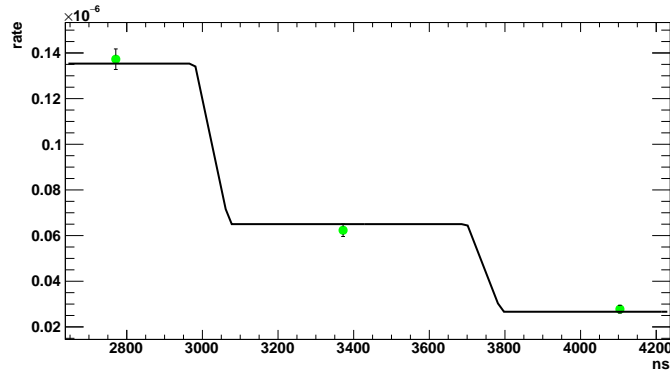


Figure 4.24: Rate vs time with fit function in black, T=300 K.

where  $N_a$  is the Avogadro number. The normalised density is:

$$\phi = \frac{pN_a}{RTN_0}. \quad (4.9)$$

Considering  $P = 40.46$  atm, and  $T = 307$  K the value of  $\phi$  is 0.0455177.

Remaining values in equation 4.2 are taken from literature and theoretical calculations:

- $\Lambda_{pp\mu} = 2.01 \cdot 10^6 \text{ s}^{-1}$  and it is temperature independent [28];
- $\Lambda_{pd}$  is of the order of  $0.8 \cdot 10^{10} \text{ s}^{-1}$ ; notice that  $\Lambda_{pd}$  is temperature dependent and I used a theoretical estimate for its value at each temperature [27];
- $\lambda_0 = (4556.01 \pm 0.14) \cdot 10^2 \text{ s}^{-1}$  [28, 36].

## 4.5.2 Fit of the data

The decreasing exponential plots of the rate as function of temperature were fitted with the function in equation 4.1; an example, for the data acquired at T=300 K, is presented in figure 4.24. The fit function step-like behaviour is due to the numerical integration of this function for each time bin. The transfer rate was obtained from the fit.

The procedure described in this chapter, from the data correction determination to the calculation of the transfer rate, was repeated for all the temperatures.

The measured transfer rate as function of T is shown in figure 4.25, red points. Black points represent the measured obtained by FAMU using LaBr3(Ce) detectors. The open point is the result obtained at PSI [47]. The grey region represents the systematic errors evaluated in this work (see section 4.6).

The statistical error is almost constant for all the points. Systematic errors are asymmetric as explained in the next section.

Considering both the systematic and statistical error, the results obtained with the fast HPGe are in agreement with the ones found using LaBr3(Ce).

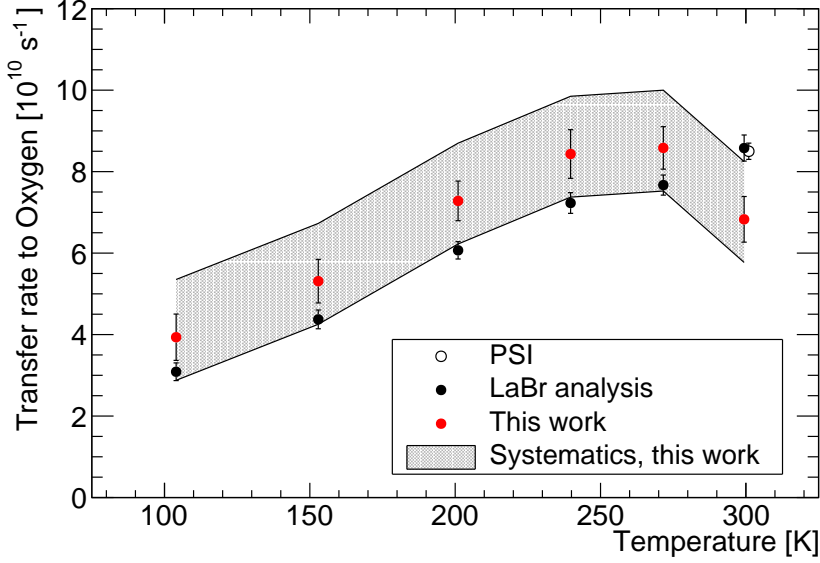


Figure 4.25: Transfer rate as function of temperature. Black points are the result of this analysis, the red points are the result obtained considering LaBr3(Ce) detectors. The grey region indicates the systematic error contribution. The empty point represents the result obtained at PSI.

## 4.6 Systematic errors estimation

The estimate of systematic uncertainties is fundamental to determine the accuracy of the measurement. In this work, the dominant sources of systematic error are due to the efficiency correction determination and to the background subtraction; other error sources are the gas concentration evaluation, other uncertainties related to the software reconstruction, the use of parameters with an associated error and the temperature measurement.

### 4.6.1 Background subtraction

I subtracted the background evaluated with the  $H_2 + CH_4$  mixture.

The background can also be determined using spectroscopic algorithms embedded in ROOT [48]. I used this algorithm to estimate the background in [100, 330] keV, that is the same energy range used in the analysis.

Both the subtraction methods give a similar trend in the transfer rate measured as function of T. The ROOT algorithm, however, depends on statistical fluctuations of each time and temperature bin. The measured transfer rate differs, respect to the smoothed  $H_2 + CH_4$  background algorithm of about  $\begin{matrix} +20\% \\ -13\% \end{matrix}$ .

These values have been considered as the estimation of systematic error due to background subtraction.

## 4.6.2 Efficiency correction

As described in section 4.3, I calculated the efficiency correction following two different methods; finally I decided to use the one that over estimates the correction, based on the  $\Delta RT < 400$  ns cut.

To estimate the efficiency correction systematic error I repeated the analysis using the first method, the one I previously discarded.

The transfer rate values are systematically lower than those found with the first correction. This means that this correction has the effect of lower the transfer rate curve. The correction itself is important in the prompt phase, when it amounts to  $\approx 60\%$  in the range [1200, 2200] ns, and it becomes less significant in the delayed phase.

In this analysis I considered events that occurred after 2500 ns, where this correction is less relevant and the associated systematic error is estimated to be -7%.

## 4.6.3 Concentration of gas mixture

The gas used was certified by the producer as high purity gas, 99.9995% and 99.9999% pure, corresponding to a contamination of other gases smaller than 5 and 1 ppm. However, the gas mixture was prepared by the producer by weight with a relative error of 3%. The uncertainty on the concentration is reflected in a systematic error on the determination of  $\Lambda_{pO_2}$  since the concentration it is one of the fit parameters. The error contribution to  $\Lambda_{pO_2}$  determination is about 3%.

## 4.6.4 Temperature

In 2016 FAMU apparatus there was a precise temperature control, as described in chapter 3. The error on temperature evaluation is about 2% and it is mainly due to the target filling procedure, because, during the target filling the temperature was not constant, whereas the pressure was under control. The temperature indetermination is reflected also in the gas density  $\phi$  that is one of the fit parameters. The systematic contribution to the final measurement is about 2%.

## 4.6.5 $t_{th}$ uncertainty

As discussed in section 4.2, the rise time distribution has a time spread of about 40 ns. To calculate the systematic error contribution I considered the efficiency correction curve (obtained by  $\Delta RT$  distribution), shifting it of 20 ns to the left and to the right. The systematic error is about of 0.4% that is negligible.

## 4.6.6 Other systematics

To perform the transfer rate measurement I used values taken from literature and from theoretical calculation. In both cases the following quantities gives a negligible contribution to the systematic error:

- oxygen and deuterium concentration  $c_{O_2}$ ,  $c_d$ ;
- the liquid hydrogen number density  $N_0$ ;
- $\Lambda_{pp\mu}$ , formation rate of molecular  $pp\mu$ ;
- $\Lambda_{pd}$ , muon transfer from  $\mu p$  to deuterium;
- $\Lambda_0$ , rate of disappearance of the muons bounded to proton.

Finally, the pile up events the software is not able to reconstruct are analysed as one signal with higher energy. This aspect introduces an uncertainty that will be better quantified by means of the simulation, currently under study.

## 4.7 Results discussion

The results of this work, taking into account both the statistical and the systematic errors, are summarised in table 4.1 and shown in figure 4.25.

T (K)	$\Lambda_{pO_2}(\times 10^{10}s^{-1})$	stat ( $\times 10^{10}s^{-1}$ )	sys ( $\times 10^{10}s^{-1}$ )
299.4	6.8	$\pm 0.6$	+1.4 -1.1
271.6	8.6	$\pm 0.5$	+1.4 -1.1
239.7	8.4	$\pm 0.6$	+1.4 -1.1
201.0	7.3	$\pm 0.5$	+1.4 -1.1
152.9	5.3	$\pm 0.5$	+1.4 -1.1
104.0	3.9	$\pm 0.6$	+1.4 -1.1

Table 4.1: Summary of the measurement results with the associated statistical and systematic errors.

The measured transfer rate is in good agreement with LaBr3(Ce) analysis results and previous measurement. Even considering statistical and systematic uncertainties, a dependence of the transfer rate as function of the temperature is confirmed. This effect is fundamental for the final measurement: the goal is to set the measurement conditions such as pressure and temperature to exploit the energy dependence of the muon transfer rate from hydrogen to higher Z atoms at epithermal energies.

This analysis not only confirmed independently the LaBr3(Ce) results but also set the basis for a deeper study of the HPGe signals. Statistic can be improved by analysing also the other three HPGe detectors. Systematic uncertainties could be reduced by further developing the GEANT4 simulation and by comparing the data of different HPGe and by exploiting their different positions around the target.

Finally, this work will help in the definition and set up of the target and detectors for the spectroscopic measurement foreseen in 2018/2019.

# Chapter 5

## Conclusions

In this thesis I presented the problem of the proton radius determination that is a current issue especially in the last ten years because of the large discrepancy between the measurement results. Infact both for the charge and for the Zemach radius, obtained with scattering experiments or with spectroscopic techniques, using electrons or muons, the results differ up to  $7\sigma$ . In particular, for the Zemach radius, only few experiments were performed using spectroscopic techniques: the FAMU experiment is placed in a fervent context proposing to obtain the proton Zemach radius by measuring the hyperfine energy splitting of the muonic hydrogen ground state. This energy is too small to be detected directly, therefore the experiment exploits the muon transfer rate from the muonic hydrogen,  $\mu p$ , to another heavy  $Z$  atom present in the gas mixture which behaviour shares an energy dependence. If at higher energies the transfer rate is faster, this property can be used to set the physical conditions to obtain the maximum transfer rate at the hyperfine energy value.

To verify and to determine the energy dependence of the  $\mu p$  transfer rate is fundamental to obtain the best result with great accuracy (less than 1%).

The aim of my analysis was the determination of the muon transfer rate from  $\mu p$  to oxygen in a gas mixture of  $H_2 + 0.3\%O_2$  at constant density  $\phi$  as function of the target temperature using the data acquired with a HPGe fast shaping. Moreover, this study is important to perform an independent analysis respect to the one made with the LaBr3(Ce) detectors to verify the results also because the systematics due to the detectors are different.

In my analysis I applied two corrections on the data: the first, called dead time correction, due to the saturation of the electronics that causes a loss of events. The maximum number of lost events is of about 20% in a time interval corresponding to the prompt phase. The second correction, called the pile up rejection, is larger than the dead time correction, about 80% in the prompt phase. These two corrections are fundamental to reconstruct the correct number of events in the energy spectrum as function of time.

These two corrections are important in the prompt time region, whereas in the delayed one, in which this analysis is performed, are less significant. Unexpectedly, the major contribution to the error comes from the background determ-

ination especially in the energy range in which there are the oxygen lines.

Studying the time evolution of the delayed oxygen emission I obtained the transfer rate for each temperature; to balance the lack of statistics in the energy spectra I considered only three time intervals.

For each temperature the data were fitted with a function that takes into account also the formation rate of  $pp\mu$  and  $p\mu d$  molecules. The statistical error accounts for about the 8% of the measurements.

A study of the systematic uncertainties was performed: the major contribution is due to the background subtraction, about 20%; other contributions come from the efficiency correction (7%), from the determination of the gas concentration (3%) and of the temperature (2%). The uncertainty on  $t_{th}$  and on the fit function parameters are evaluated and considered negligible.

The final result is in agreement with the one obtained with the LaBr3(Ce) data and it shares a dependence of the transfer rate from temperature.

Knowing this dependence will permit to fix the best experimental conditions to perform the measurement of the hyperfine energy splitting of the muonic hydrogen atom ground state using the laser source.

In the next phase the optical cavity will be placed in the gas target and, together with the mid-infrared laser, the FAMU collaboration will perform the final measurement to obtain the resonance plot and so the proton Zemach radius.

# Bibliography

- [1] H. Geiger and E. Marsden, *On a Diffuse Reflection of the  $\alpha$ -Particles*, in *Proc. R. Soc. A*, **82** (1909).
- [2] J.J. Thomson, *On the Structure of the Atom: an Investigation of the Stability and Periods of Oscillation of a number of Corpuscles arranged at equal intervals around the Circumference of a Circle; with Application of the Results to the Theory of Atomic Structure*, *Phil. Mag. Series 6*, **7**, Issue 39 (1904).
- [3] E. Rutherford, *Collision of  $\alpha$  particles by matter and the structure of the atom*, *Phil. Mag.*, **90** (1919).
- [4] R. Pohl et al., *The size of proton*, *Nature*, **466** (2010).
- [5] P. J. Mohr, D. B. Newell, and B. N. Taylor, *CODATA recommended values of the fundamental physical constants: 2014*, *Rev. Mod. Phys.*, **88**, Issue 3 (2016).
- [6] S. Braibant, G. Giacomelli and M. Spurio, *Particles and fundamental interactions, An introduction to Particle Physics*, Springer (2012).
- [7] D. Guffanti, *The FAMU experiment: measurement of muonic atoms spectra*, Master thesis, Università degli studi dell'Insubria, (2015).
- [8] URL: [http://www.roma1.infn.it/people/luci/fns/scattering\\_elastico\\_ep.pdf](http://www.roma1.infn.it/people/luci/fns/scattering_elastico_ep.pdf)
- [9] J. C. Bernauer et al., *High-Precision Determination of the Electric and Magnetic Form Factors of the Proton*, *Phys. Rev. Lett.*, **105** (2010).
- [10] A. Gasparian et al., *High Precision Measurement of the Proton Charge Radius*, An Update to Proposal C12-11-106 for Jefferson Lab PAC-39.
- [11] Michael Kohl on behalf of the MUSE collaboration, *The Muon Scattering Experiment (MUSE) at PSI and the proton radius puzzle*, *EPJ Web Conference*, **81** (2014).
- [12] J. C. Bernauer, *The Precision Frontier in Lepton-Proton Scattering*, in *International Conference on Precision Physics and Fundamental Physical Constants*, (FFK-2017), 15-19.05.2017, Warsaw, Poland.

- [13] W. E. Lamb and R. C. Retherford, *Fine Structure of the Hydrogen Atom by a Microwave Method*, *Phys. Rev.*, **73**, Issue 3 (1947).
- [14] A. Antognini, *The Lamb shift experiment in muonic hydrogen*, PhD thesis, Ludwig-Maximilians-Universität München, (2005).
- [15] R. Pohl, *Laser spectroscopy of muonic atoms*, in *International Conference on Precision Physics and Fundamental Physical Constants*, (FFK-2017), 15-19.05.2017, Warsaw, Poland.
- [16] R. Pohl et al., *Laser spectroscopy of muonic deuterium*, *Science*, **353** (2016).
- [17] Julian J. Krauth on behalf of the CREMA collaboration, *The Lamb shift measurement in muonic helium ions*, in *International Conference on Precision Physics and Fundamental Physical Constants*, (FFK-2017), 15-19.05.2017, Warsaw, Poland.
- [18] A. C. Zemach, *Proton Structure and the Hyperfine Shift in Hydrogen*, *Phys. Rev.* **6**, **104** (1956).
- [19] B. H. Bransden and C. J. Loachain, *Physics of atoms and molecules*, *Longman Scientific & Technical*, (1983).
- [20] A. Dupays et al., *Proton Zemach radius from measurements of the hyperfine splitting of hydrogen and muonic hydrogen*, *Phys. Rev. A*, **68** (2003).
- [21] J. L. Friar and I. Sick, *Zemach moments for hydrogen and deuterium*, *Phys. Lett. B*, **579** (2004).
- [22] M. Sato et al., *Laser Spectroscopy of Ground State Hyperfine Splitting Energy of Muonic Hydrogen*, *JPS Conf. Proc.*, **8** (2015).
- [23] A. Antognini, *Hyperfine splitting in  $\mu p$  and  $\mu^3\text{He}^+$* , *International Conference on Precision Physics of Simple Atomic Systems*, Jerusalem (2016).
- [24] R.N.Faustov and A.P.Martynenko, *Muonic hydrogen ground state hyperfine splitting*, URL: <https://arxiv.org/pdf/hep-ph/0312116.pdf> (2004).
- [25] A. Adamczak et al., *Steps towards the hyperfine splitting measurement of the muonic hydrogen ground state: pulsed muon beam and detection system characterization*, *JINST*, **114** (2016).
- [26] D. Bakalov et al., *Theoretical and computational study of the energy dependence of the muon transfer rate from hydrogen to higher-Z gases*, *Phys. Lett. A*, **379**, Issue 3 (2015).
- [27] A. Adamczak, calculation based on C. Chiccoli et al., *Muon Catal. Fusion* **7**, **87** (1992).

- [28] V. A. Andreev et al., *Measurement of the formation rate of muonic hydrogen molecules*, *Phys. Rev. C*, **91** (2015).
- [29] D. Bakalov et al., *Experimental method to measure the hyperfine splitting of muonic hydrogen  $(\mu^- p)_{1S}$* , *Phys. Lett. A*, **172** (1993).
- [30] D. Bakalov and A. Adamczak, FAMU internal note.
- [31] URL: <http://www.stfc.ac.uk/about-us/where-we-work/rutherford-appleton-laboratory/>.
- [32] URL: <http://www.isis.stfc.ac.uk/groups/riken-ral/riken-ral-muon-group7618.html>.
- [33] T. Matsuzaki et al., *The RIKEN-RAL pulsed Muon Facility*, *Nucl. Inst. & Meth. A*, **465** (2001).
- [34] URL: <http://www.criotec.com>.
- [35] K.A. Olive et al., *Particle Data Group*, *Chin. Phys.*, **C38** (2014),  
URL: <http://pdg.lbl.gov>.
- [36] T. Suzuki, D. F. Measday, J. P. Roalsvig, *Total nuclear capture rate for negative muons*, *Phys. Rev. C*, **35** (1987).
- [37] Luigi Pio Rignanese, *Sviluppo di un sistema di rivelazione per l'esperimento FAMU (Fisica degli Atomi Muonici) basato su scintillatore LaBr<sub>3</sub> con fotomoltiplicatore UQE e sistema spettrometrico DSP*, Master thesis, Università di Bologna, (2015).
- [38] Hamamatsu Photonics, *R11265U data sheet*, URL: [https://www.hamamatsu.com/resources/pdf/etd/R11265U\\_H11934\\_TPMH1336E.pdf](https://www.hamamatsu.com/resources/pdf/etd/R11265U_H11934_TPMH1336E.pdf).
- [39] G. Baldazzi et al., *The LaBr<sub>3</sub>(Ce) based detection system for the FAMU experiment*, *JINST*, **12** (2017).
- [40] BrillanCeTM Scintillators Performance Summary,  
URL: [http://www.crystals.saint-gobain.com/sites/imdf.crystals.com/files/documents/brilliance\\_scintillators\\_performance\\_summary\\_69795.pdf](http://www.crystals.saint-gobain.com/sites/imdf.crystals.com/files/documents/brilliance_scintillators_performance_summary_69795.pdf).
- [41] Glenn F. Knoll, *Radiation detection and measurement*, *John Wiley & Sons* (2000).
- [42] M. Bonesini et al., *The proton radius puzzle*, *JINST*, **12** (2017).
- [43] AdvanSiD, *ASD-RGB3S-P datasheet*,  
URL: [http://advansid.com/attachment/get/up\\_53\\_1432741078.pdf](http://advansid.com/attachment/get/up_53_1432741078.pdf).
- [44] URL: <http://www.lakeshore.com>.

- [45] Sumitomo (SHI) Cryogenics of America, *CH-104 and CH-110 Cold Heads Operating Manual* (2010).
- [46] C. Boschi and I. Baneschi, measurement of the gas isotopic composition performed at IGG, CNR Pisa.
- [47] A. Werthmüller et al., *Energy dependence of the charge exchange reaction from muonic hydrogen to oxygen*, *Hyp. Interact.*, **116** (1998).
- [48] R. Brun and F. Rademakers, *ROOT - An Object Oriented Data Analysis Framework*, *Nucl. Inst. & Meth. in Phys. Res. A*, **389** (1997).  
See also URL: <http://root.cern.ch/>.

# Acknowledgments

Many people deserve a sincere thanks for the contribution and help in the realisation of this thesis.

First of all, a special thanks goes to prof. Emiliano Mocchiutti, this thesis supervisor, for the patience and the willingness, for having me introduced in the FAMU collaboration and for the clarifications of my many doubts; thank for the practical teachings and for the long conversations about the future.

A sincere gratitude goes to the FAMU collaboration for the kind welcome; a particular thanks goes to prof. Andrea Vacchi to let me actively participate to the experiment both in situ and to the discussions; to Daniele e Luigi for their help to enter in the collaboration sharing with me part of their experience and for their prompt answer to my many calls; a thanks goes to Massi that with his experience resolved a lot of my doubts on the data analysis, and to Cecilia that with her corrections and observations has contributed to improve this thesis.

To all of my friends, the old and the new, for their support, thank you!

Last but not least, my family and Luca deserve a huge thanks: they supported me all my choices and they believed in me making me feel loved.

Trieste, September 2017

Elena Furlanetto